Journal of Catalysis 395 (2021) 210–226

Contents lists available at ScienceDirect

Journal of Catalysis

journal homepage: www.elsevier.com/locate/jcat

Effects of Brønsted acid site proximity in chabazite zeolites on OH infrared spectra and protolytic propane cracking kinetics

Philip M. Kester [a,1], Jerry T. Crum [b,1], Sichi Li [b], William F. Schneider [b,c,*], Rajamani Gounder [a,*]

[a] Charles D. Davidson School of Chemical Engineering, Purdue University, 480 Stadium Mall Drive, West Lafayette, IN 47907, USA
[b] Department of Chemical and Biomolecular Engineering, University of Notre Dame, 250 Nieuwland Science Hall, Notre Dame, IN 46556, USA
[c] Department of Chemistry and Biochemistry, University of Notre Dame, 251 Nieuwland Science Hall, Notre Dame, IN 46556, USA

ARTICLE INFO

Article history:
Received 5 October 2020
Revised 15 December 2020
Accepted 20 December 2020
Available online 27 January 2021

Keywords:
Acidic zeolites
Infrared OH spectra
Protolytic alkane cracking
Proton proximity
Sodium titration

ABSTRACT

The arrangement of framework Al heteroatoms in zeolite lattices influences the energetics of proton siting and thus the distribution of protons among crystallographically-distinct oxygen atoms and void environments, as shown here for H-CHA zeolites of fixed bulk Al content (Si/Al = 15) but varying amounts of proximal Al sites (Al-O-(Si-O)$_x$-Al, x = 1,2) in a six-membered ring (6-MR). Stretching vibrations of Brønsted acidic OH groups give rise to composite infrared (IR) features whose shapes and integrated intensities are invariant with temperature (448–748 K) on H-CHA zeolites containing predominantly 6-MR isolated Al sites. In sharp contrast, IR peak shapes change and integrated OH areas decrease reversibly with increasing temperature on H-CHA zeolites containing 6-MR paired Al sites (quantified by Co^{2+} titration). Periodic density functional theory (DFT) calculations show that the four distinct OH configurations at an isolated Al site exhibit distinct vibrational frequencies and molar absorptivities, but are isoenergetic (within 10 kJ mol^{-1}) rendering equilibrium proton populations and OH IR spectra insensitive to temperature. In contrast, paired proton configurations differ in energy by up to ~40 kJ mol^{-1}, with higher energy configurations having lower oscillator strengths; as a result, increasing temperatures shift proton populations toward higher energy configurations that result in a decrease in composite OH IR peak areas. First-order rate constants of protolytic propane cracking (748 K, per H^+) are ~12× higher on paired than isolated protons, despite similar apparent activation energies, reflecting apparent activation entropies that are less negative at paired proton sites. Propane cracking rates (748 K, per g) decrease linearly with Na^+ content upon partial titration of H^+ sites in CHA zeolites containing 6-MR isolated sites, but decrease more strongly at low Na^+ contents on CHA zeolites containing 6-MR paired sites, consistent with experimental OH IR spectra and DFT calculations evincing the preferential exchange of Na^+ at 6-MR paired Al sites. These conclusions about proton proximity, founded on the interrogation of well-defined and characterized CHA zeolite samples by experiment and theory, provide new insights regarding its consequences for the temperature sensitivity of OH IR spectra and protolytic alkane cracking rates in Brønsted acidic zeolites. The finding that proximal proton sites accelerate high-temperature alkane activation turnovers via non-polar transition states represents a mechanistically distinct extension of our prior reports, wherein proximal protons accelerate low-temperature alkanol dehydration turnovers via polar transition states stabilized by hydrogen bonding interactions, heralding the catalytic diversity among zeolites containing different framework Al arrangements.

1. Introduction

The location and distribution of Brønsted acidic OH groups among the distinct rings and void environments present in a zeolite framework depends on the distribution of Al heteroatoms substituted in lattice tetrahedral sites (T-sites), because charge-compensating protons are localized to the four bridging O atoms that connect $[AlO_2]^-$ tetrahedra to their corner-sharing SiO_2 tetrahedra [1,2]. In general, the siting of Al among symmetry-distinct

* Corresponding authors at: Department of Chemical and Biomolecular Engineering, University of Notre Dame, 250 Nieuwland Science Hall, Notre Dame, IN 46556, USA (W.F. Schneider); Charles D. Davidson School of Chemical Engineering, Purdue University, 480 Stadium Mall Drive, West Lafayette, IN 47907, USA (R. Gounder).
E-mail addresses: wschneider@nd.edu (W.F. Schneider), rgounder@purdue.edu (R. Gounder).
[1] P. M. K. and J. T. C. contributed equally to this work.

https://doi.org/10.1016/j.jcat.2020.12.038
0021-9517/

T-sites or in different arrangements in zeolite lattices is not determined randomly or arbitrarily, but depends on synthetic conditions including the identity and amounts of the structure directing agents (SDAs) used to guide zeolite crystallization [3]. This dependence provides a strategy to design synthetic routes to influence the atomic-level structure of zeolite materials, even for a fixed framework topology and elemental composition (i.e., Si/Al ratio), by altering the incorporation of heteroatoms into specific siloxane rings and within certain confining void environments. In turn, this structural control provides a mechanism by which to influence catalytic reactivity, via the stabilization of reactive intermediates and transition states by van der Waals [4–7] and hydrogen-bonding [8,9] interactions with framework oxygen atoms and other proton sites in the confining environment. For example, this strategy has been demonstrated for FER zeolites (Si/Al = 10–17) synthesized with tetramethylammonium and cyclic amines as organic co-SDAs to vary the fraction of proton sites located in smaller 8-membered ring (8-MR) voids [10], which stabilize transition states for dimethyl ether carbonylation more effectively via van der Waals interactions than larger 10-MR voids [11,12].

Interpretations of catalytic phenomena at distinct proton sites in zeolites must also consider proximal site arrangements [3,13], which have been proposed to influence rates of protolytic alkane cracking and dehydrogenation [14] and propene oligomerization [15,16] on MFI zeolites. Protolytic *n*-alkane (C_3-C_5) cracking and dehydrogenation rates (783–863 K, per H^+) were higher on H-MFI zeolites with lower bulk Si/Al ratios, which were able to exchange increasing amounts of Co^{2+} cations that are proposed titrants of proximal Al sites in 5- and 6-MR (Al-O-(Si-O)$_x$-Al, x = 1,2) [3,17]. With increasing proximal Al content, apparent activation energies remained similar but apparent activation entropies became systematically less negative, leading Ding and co-workers to propose that carbonium ion-like transition states formed at proximal acid sites occurred later along their reaction coordinates and were more product-like [14]. Similar trends in apparent *n*-butane cracking and dehydrogenation rate constants, activation energies, and activation entropies among MFI samples of increasing Al density were reported by Bell and co-workers [18], who instead interpreted these trends to reflect the entropic benefits conferred upon looser confinement of transition states within larger MFI channel intersections, based on Al locations inferred from deconvolution of d-d transition bands in UV–visible spectra of Co^{2+}-form MFI zeolites. The consequences of proton proximity in zeolites for turnover rates of acid-catalyzed reactions have thus remained imprecisely understood, in part because of the diversity of Al–Al pair configurations present within the low-symmetry (12 T-site) MFI framework and its various void environments (straight and sinusoidal 10-MR channels, and their intersections) that can be titrated by Co^{2+} cations [17].

CHA zeolites thus serve as a model material to interrogate acid site proximity effects in zeolites because they contain only one crystallographically-distinct T-site, simplifying the interpretation of experimental data and facilitating the construction of structural models by theory that more faithfully describe experiment. Density functional theory (DFT) calculations indicate that Co^{2+} cations preferentially titrate Al pairs within the same 6-MR in CHA over other Al–Al pair sites separated by one or two Si atoms [19], constituting evidence that supports the development and use of experimental Co^{2+} titration protocols to quantify 6-MR paired Al sites in CHA [20,21]. In prior work, we reported methods to synthesize CHA zeolites with essentially fixed composition (Si/Al ~ 15) but systematic variations in the percentage of Al atoms present in 6-MR site pairs (0–44%), using mixtures of *N,N,N*-trimethyl-1-admantylammonium ($TMAda^+$) and Na^+ cations as co-SDAs; $TMAda^+$ becomes occluded within the CHA cage and Na^+ cations become co-occluded within adjacent 6-MRs to provide an energetic preference to stabilize 6-MR paired Al arrangements [19]. Turnover rates of bimolecular methanol dehydration to dimethyl ether [21] and ethanol dehydration to diethyl ether [8] were up to ~20× higher (415 K, per H^+) on 6-MR paired protons than isolated protons in CHA, consistent with DFT calculations showing that the anionic charge distributions provided by these specific Al arrangements preferentially stabilize the cationic transition states formed in alkanol dehydration via hydrogen bonding interactions with co-adsorbed alkanol molecules at the second acid site [8].

Infrared spectra of OH stretches can be used to directly interrogate the structure and distribution of Brønsted acid sites in zeolites, yet several challenges complicate such assessments. Multiple OH stretching features can be present even for the simplest case of an isolated Al site, given that bridging framework oxygens are typically symmetry-distinct and occupy different void environments. Thus, IR spectra may exhibit multiple OH vibrational stretching features in the nominally isolated Al limit, even in frameworks that contain a single symmetry-distinct T-site such as CHA. Vibrational features become invariably more complex with heterogeneities introduced by multiple distinct T-sites in lower-symmetry frameworks and by interactions between proximal Al sites that are present even in high-symmetry frameworks. Göltl et al. showed that CHA samples varying Si/Al ratios (6, 12, 35) contained two features associated with Brønsted acidic OH stretches and that these features varied systematically in relative intensity with composition, which was rationalized in terms of the increasing contributions of proximal sites with decreasing Si/Al ratio, as supported by DFT models of the spectral features of isolated and proximal site types [22]. Additionally, the intensities of OH IR features are sensitive to local environment, complicating efforts to quantify sites based on observed spectra. Empirically, this sensitivity is reflected in measurements of molar attenuation coefficients that vary widely (2–20 cm μmol^{-1}) among H-form zeolites of different topology (e.g., MFI, FAU, MOR) [23–27]. Heuristic arguments suggest that OH groups confined within smaller rings are more strongly perturbed by hydrogen bonding interactions with O-atoms in the ring, leading to lower stretching frequencies [28] and higher molar attenuation coefficients because charge transfer through H-bonds increases oscillator strength [29,30]. These general heuristics would suggest, at first glance, that the IR features observed at 3575 and 3600 cm^{-1} in H-CHA reflect OH stretches oriented within the plane of the 6-MR and 8-MR, respectively [31]. We show here that such interpretations do not precisely describe the structural properties of zeolites that give rise to IR OH stretching vibrational spectra, which becomes evident from examining the simplest case of an isolated Al site in a single T-site CHA lattice.

Here, we use IR spectroscopy and supercell DFT models to probe the arrangement of protons among the four bridging O atoms in framework Al tetrahedra in isolated and paired site configurations in CHA zeolites, exploiting samples synthesized specifically to contain varying fractions of 6-MR paired Al sites at fixed bulk composition (Si/Al ~ 15). Experimentally observed and modeled IR spectra of bridging OH groups at 6-MR paired Al sites decrease in intensity with increasing temperature (448–748 K) as proton configurations that are higher in energy and that have lower oscillator strengths contribute more substantially to observed spectra. In contrast, the four OH groups associated with an isolated Al site are isoenergetic and result in IR spectra that are insensitive to temperature. We use protolytic propane cracking as a probe reaction that prevails under conditions wherein Brønsted acid active sites remain uncovered during catalysis. Apparent first-order rate constants (per total H^+, 748 K) systematically increase with the fraction of 6-MR paired Al sites and are ~12× larger at paired than isolated protons, reflecting less negative apparent activation entropies at

paired sites, providing evidence that proximal acid sites entropically stabilize carbonium-ion-like transition states, consistent with prior reports on H-MFI zeolites [14]. DFT calculations and experimental data indicate that Na^+ cations preferentially titrate protons at 6-MR paired Al configurations; as a result, protolytic propane cracking rates (per initial H^+, 748 K) decrease more strongly with Na^+ content on CHA samples that contain 6-MR paired sites than the equimolar titration behavior observed on CHA samples that contain isolated Al sites. These findings unambiguously reveal the heterogeneities in proton siting dictated by the arrangement of framework Al atoms in zeolite lattices, which engender changes in reactivity for hydrocarbon catalysis that prevails at high temperatures on predominantly bare proton sites.

2. Methods and materials

2.1. Synthesis and post-synthetic treatments of CHA zeolites

CHA zeolites were synthesized hydrothermally according to methods reported by Di Iorio and Gounder [20] from synthesis media comprised of molar ratios of 1 SiO_2/ 0.0333 Al_2O_3/ 0.5-x TMAdaOH/ x NaOH/ 44 H_2O, where x varied between 0 and 0.25. In a typical synthesis, a 1 M TMAdaOH solution (25 wt%, Sachem) was diluted with deionized water (18.2 MΩ·cm) in a perfluoroalkoxy alkane (PFA) container (Savillex Corp.) and stirred for 15 min under ambient conditions. Then, $Al(OH)_3$ (98 wt%, SPI Pharma) or Al(*i*-o-Pr)$_3$ (98 wt%, Sigma-Aldrich) was added to the solution and stirred for 15 min under ambient conditions. NaOH (98 wt%, Alfa Aesar) was then added to the mixture and homogenized for 15 min. Finally, colloidal silica (Ludox HS 40, 40 wt%, Sigma-Aldrich) was added and the solution was stirred for 2 h under ambient conditions to homogenize its contents. The solution was then placed in a 45 mL Teflon-lined stainless-steel autoclave (Parr Instruments) and heated in a forced convection oven (Yamato DKN-402C) at 433 K and rotated at 40 rpm for 144 h. Recovered solids were washed with deionized water and mixtures of deionized water and acetone (99.999%, Sigma-Aldrich) (50%/50% (w/w)) in alternating steps (70 g solvent (g solid)$^{-1}$ per wash) and separated by centrifugation until the pH of the supernatant liquid was constant, then dried for 24 h at 373 K in stagnant ambient air. Organic SDAs were removed by treatment under flowing dry air (1.67 cm^3 s^{-1} g_{cat}^{-1}, 99.999% UHP, Indiana Oxygen) at 853 K (0.0167 K s^{-1}) for 10 h.

2.2. Preparation of monovalent and divalent cation-exchanged CHA zeolites

Aqueous-phase ion-exchange procedures were performed as reported by Di Iorio and Gounder [20]. Following removal of occluded organic SDAs, residual Na^+ cations were removed by aqueous-phase ion-exchange in a 1.0 M NH_4NO_3 solution (8.0 wt % in deionized H_2O, 100 cm^3 (g solid)$^{-1}$; 99.9 wt%, Sigma-Aldrich) for 24 h at ambient conditions. Solids were recovered via centrifugation and washed with deionized water four times (70 cm^3 (g solid)$^{-1}$), then dried at 373 K for 24 h under stagnant ambient air. NH_4-form samples were converted to their H-form by treatment in flowing dry air (1.67 cm^3 s^{-1} g_{cat}^{-1}, 99.999% UHP, Indiana Oxygen) at 773 K (0.0167 K s^{-1}) for 4 h to obtain H-form samples.

H-CHA zeolites were converted to their Co^{2+}-form by ion-exchange in aqueous $Co(NO_3)_2$ solutions (0.25 M $Co(NO_3)_2$ in deionized water, 100 cm^3 (g solid)$^{-1}$; 99 wt%, Sigma-Aldrich) for 4 h at ambient conditions under 300 rpm stirring. Samples were then washed with deionized water four times (70 cm^3 (g solid)$^{-1}$), then dried at 373 K for 24 h under stagnant ambient air. Co^{2+}-form samples were then treated in flowing dry air (1.67 cm^3 s^{-1} g_{cat}^{-1}, 99.999% UHP, Indiana Oxygen) at 773 K (0.0167 K s^{-1}) for 4 h.

NH_4-CHA zeolites were partially exchanged with Na^+ cations in aqueous NaCl solutions (0.01–0.15 M, 100 cm^3 (g solid)$^{-1}$; 98 wt%, Macron) for 24 h under ambient conditions. Na^+-exchanged samples were washed four times in deionized water (70 cm^3 (g solid)$^{-1}$), then dried at 373 K for 24 h under stagnant ambient air. Na-H-form samples were then treated in flowing dry air (1.67 cm^3 s^{-1} g_{cat}^{-1}, 99.999% UHP, Indiana Oxygen) at 773 K (0.0167 K s^{-1}) for 4 h.

2.3. Physicochemical characterization of CHA zeolites

Crystal structures of CHA zeolites were verified after removal of organic SDAs with powder X-ray diffraction (XRD) patterns using a Rigaku SmartLab X-ray diffractometer with a Cu Kα radiation source operating at 1.76 kW. In a typical experiment, 0.01 g of CHA were loaded into a zero-background, low-dead-volume sample holder (Rigaku) and diffraction patterns were collected at a scan rate of 0.0167° s^{-1} and a step size of 0.01°.

Micropore volumes were calculated from Ar adsorption isotherms (87 K) measured with a Micromeritics ASAP 2020 surface area and porosity analyzer. CHA zeolites (0.03–0.05 g, sieved to 180–250 μm) were degassed under vacuum (5 μmHg) at 393 K for 2 h, followed by heating to 623 K (0.167 K s^{-1}) under vacuum (less than 5 μmHg) for 9 h. The volumetric uptake of Ar (0.05–0.35 P/P_0) was used to estimate micropore volumes (cm^3 (g solid)$^{-1}$ at STP). These micropore volumes were similar (±10%) to those calculated from the first minimum in a semilogarthmic derivative plot of the isotherm, given by $\partial(V_{ads})/\partial(\ln(P/P_0))$ vs $\ln(P/P_0)$.

Elemental compositions of CHA zeolites were determined with atomic absorption spectroscopy (AAS) with a PerkinElmer Model AAnalyst 300 atomic absorption spectrometer. Aqueous samples were prepared by dissolving ~0.03 g of solid in 2 g of hydrofluoric acid (48 wt%, Alfa Aesar) and allowed to sit for 24 h, then diluted in 50 g of deionized water. *[Caution: when working with HF acid, use appropriate personal protective equipment, ventilation, and other safety precautions].* Absorbances were measured with radiation sources at wavelengths of 309.3 nm in a reducing acetylene/nitrous oxide flame for Al, and wavelengths of 589.0 nm and 240.7 nm for Na^+ and Co^{2+}, respectively, in an oxidizing air/acetylene flame. Elemental compositions were calculated from calibration curves obtained from absorbances measured from known standards.

The total number of Brønsted acid sites on zeolite samples was estimated by NH_3 temperature-programmed desorption (TPD); NH_3 titration of protons in H-CHA was performed via aqueous-phase ion-exchange (ca. 298 K) with NH_4^+ cations, while in Na-H-CHA samples was performed via gas-phase titration with NH_3 (433 K) and subsequent wet He purging methods described previously [32–34]. NH_4-form (or Na-NH_4-form) samples (0.02–0.05 g, sieved to 180–250 μm) were loaded into a U-shaped quartz reactor and supported with quartz wool, then placed in a clam-shell furnace in a Micromeritics AutoChem II 2920 Chemisorption analyzer equipped with an Agilent 5973 N mass-selective detector. Samples were heated to 873 K (0.167 K s^{-1}) under flowing He (15 cm^3 s^{-1} (g solid)$^{-1}$), and effluent mixtures were sent to the mass-selective detector for quantification. Calibration and deconvolution methods were performed according to previous methods [32,33] to quantify the number of NH_3 molecules desorbed from zeolite samples.

2.4. Infrared spectra of OH stretching features in H-CHA and Na-H-CHA zeolites

H-CHA and Na-H-CHA zeolites were pressed into self-supporting wafers (0.02–0.04 g cm^{-1}) and sealed within a

custom-built quartz IR cell with CaF_2 windows. Details on the construction of the IR cell can be found in [35]. Zeolite wafers were treated in flowing dry air (10 $cm^3\ s^{-1}\ g_{cat}^{-1}$) purified by an FTIR purge gas generator (Parker Balston, less than1 ppm CO_2) to 803 K (0.0167 K s^{-1}) for 2 h, then cooled to 748 K under flowing He (10 $cm^3\ s^{-1}\ g_{cat}^{-1}$). IR spectra were collected with a Nicolet 4700 spectrometer with a Hg-Cd-Te detector (MCT, 77 K), and 64 scans at 2 cm^{-1} resolution were averaged in the 4000–400 cm^{-1} range at temperatures of 415–748 K. Backgrounds were subtracted with IR spectra collected with an empty IR cell under flowing He. IR spectra are normalized to the integrated area of lattice T-O-T overtone and combination modes (1750–2100 cm^{-1}), used as an internal standard for the wafer sample mass in the path of the IR beam, to accurately compare IR absorbances among different samples [36,37].

2.5. Density functional theory methods

Supercell DFT calculations were performed using the Vienna Ab-Initio Simulation Package (VASP) [38]. Electron exchange and correlation were described using the Perdew-Burke-Ernzerhof (PBE) functional [39] and core-valence interactions were modeled using the projector augmented wave method [40,41]. Plane wave energy cutoffs were set to 800 eV for lattice constant optimizations and 400 eV for all other calculations. The self-consistent field electronic calculations were considered converged when the energy change between iterations was less than 1×10^{-6} eV, and geometry optimizations continued until the maximum force on any atom was less than 0.01 eV/Å. A 36 T-site CHA supercell was obtained from the Database of Zeolite Structures [42]. The purely siliceous lattice constants were optimized by allowing ions, lattice shape, and lattice size to update; results are shown in Fig. S3 (Section S2, SI). All subsequent calculations were performed at the optimized lattice constants. Harmonic vibrational frequencies were computed using density functional perturbation theory [43]. Structure input files and modifications were constructed within the Atomic Simulation Environment [44].

2.6. Monomolecular propane cracking kinetic measurements

H-CHA or Na-H-CHA zeolites (0.02–0.10 g, sieved to 180–250 μm) were loaded into a quartz reactor (7 mm inner diameter) and supported between two plugs of quartz wool (Acros Orgnaics). Reactor temperatures were controlled with a resistively-heated three-zone furnace (Applied Test Systems Series 3210) and Watlow controllers (EZ-Zone series). Catalyst temperatures were measured with a Type K thermocouple at the external surface of the quartz reactor tube placed at the middle of the catalyst bed. Samples were treated in a stream of flowing O_2 (5 kPa O_2 with balance He, 99.999% UHP, Indiana Oxygen) or H_2 (99.999% UHP, Indiana Oxygen) at 803 K for 2 h (0.0167 K s^{-1}), then cooled to 748 K in flowing He (99.999% UHP, Indiana Oxygen) and held for 0.5 h to remove O_2 or H_2 from transfer lines. Propane (10 kPa, 5 kPa Ar, balance He, Indiana Oxygen) was diluted in He to pressures of 0.6–2.2 kPa and sent to the reactor at site contact-times of 20–30 s (mol H^+) $(\text{mol } C_3H_8)^{-1}$. Reactant and product gas-phase concentrations were measured with a gas chromatograph (HP 6890 Series) equipped with a flame ionization detector and a GS-Alumina KCl capillary column (0.53 mm inner diameter, Agilent). Propane conversions were held below 1% to mitigate secondary bimolecular reactions of product alkenes. As expected for protolytic propane cracking on Brønsted acid sites, ethene and methane products were formed in equimolar quantities (1.0 ± 0.1), and rates showed a first-order dependence on propane pressure (Fig. S10, Section S6, SI). Apparent first-order rate constants were independent of total acid site content among H-CHA samples with a given Al arrangement, and were independent of propane site contact-time (Fig. S11, Section S6, SI), respectively indicating that measured rate data were not corrupted by intracrystalline or extracrystalline transport phenomena. Apparent activation energies and entropies were calculated from propane cracking rate constants (per H^+) between 718–778 K.

3. Results and discussion

3.1. Experimental IR spectroscopic characterization of isolated and proximal protons in CHA zeolites

CHA zeolites of similar bulk composition (Si/Al ~ 15) but varying amounts of 6-MR paired Al sites, as quantified by Co^{2+} titration, were synthesized according to procedures reported by Di Iorio and Gounder [20]. In brief, CHA samples were prepared to contain predominantly 6-MR isolated Al sites by hydrothermal crystallization using only $TMAda^+$ as the organic SDA, while samples were prepared with increasing amounts of 6-MR paired Al sites by the addition of Na^+ as an inorganic co-SDA [19,20]. Table 1 summarizes the salient bulk and site properties of the CHA samples studied here, which are denoted as CHA (X, Y), where X is the Si/Al ratio and Y is the percentage of Al sites in a 6-MR paired configuration. XRD patterns (Fig. S1, SI) and micropore volumes (0.16–0.22 $cm^3\ g^{-1}$, Table 1) measured from Ar adsorption isotherms (87 K, Fig. S2, SI) were those expected for the CHA topology. Al sites were predominantly incorporated into tetrahedral lattice positions, evidenced by Brønsted acid sites quantified by NH_4^+ ion-exchange and subsequent NH_3 temperature programmed desorption (TPD) to be present in nearly equimolar ratios to the total Al content measured by atomic absorption spectroscopy (H^+/Al = 0.75–1.02, Table 1). The number of 6-MR paired Al sites was quantified by Co^{2+} titration by (i) measuring Co^{2+} ion-exchange isotherms to verify that the conditions used saturated all available exchange sites, (ii) quantifying a cation site balance to verify that each Co^{2+} exchanged two protons as determined by the number of residual H^+ sites on Co-form zeolites quantified by selective NH_3 titration, and (iii) collecting UV–Visible spectra of dehydrated Co-CHA samples that did not show features for Co-oxide species [20]. These CHA samples contain essentially the same Al content (nominal Si/Al = 15, actual Si/Al = 14–17, Table 1) but systematically different amounts of 6-MR paired Al sites, thus providing a suite of well-defined materials to study the effects of Al proximity on IR spectra and the kinetics of an acid-catalyzed reaction, without convolving any effects of Al location given that CHA contains only one T-site.

Infrared (IR) spectra of the OH stretching region, collected at 415 K and normalized to the integrated area of lattice Si-O-Si overtone and combination modes (1750–2100 cm^{-1}), are shown in Fig. 1 for five H-CHA samples of fixed bulk Al content (Si/Al = 15) but varying percentages of Al in 6-MR paired configurations. All spectra show a feature near 3740 cm^{-1} for silanol groups (Si-OH) and two features at 3575 and 3600 cm^{-1} for OH stretches for Brønsted acidic OH groups (Si-O(H)-Al), along with a small peak at 3650 cm^{-1} for OH stretches associated with minority extraframework Al sites [45]. The relative intensities of OH stretches associated with silanol groups and extraframework Al species vary among samples because of differences in crystallite sizes (SEM and DLS data reported previously [21]) and in extraframework Al content (1 – H^+/Al; Table 1), but were not interpreted further in this study because these material properties do not influence measured rates of protolytic propane cracking (additional discussion in Section S7, SI). The two features at 3575 and 3600 cm^{-1} have been previously assigned to OH groups oriented within the plane of the 6-MR and 8-MR of CHA, respectively, as determined from Rietveld refinement of neutron diffraction data collected at 5 K [31]. The component at 3600 cm^{-1} becomes more

Table 1
Elemental composition, micropore volume, and number of total H^+ sites and Al in 6-MR paired ensembles in CHA samples of essentially fixed total Al content.

Sample[a]	Si/Al[c]	H^+/Al[d]	Fraction of Al in 6-MR Pairs (2 × Co/Al)[e]	Micropore volume[f]/cm^3 g^{-1}
CHA (14.5, 0%)	14.5	0.75	0.00	0.19
CHA (16.0, 0%)	16.0	0.98	0.00	0.20
CHA (17.5, 0%)	17.5	0.99	0.00	0.21
CHA (15.5, 8%)	15.5	0.96	0.08	0.19
CHA (15.5, 13%)	15.5	0.90	0.13	0.17
CHA (14.8, 18%)	14.8	0.99	0.18	0.22
CHA (13.8, 20%)	13.8	1.02	0.20	0.20
CHA (16.2, 24%)	16.2	0.76	0.24	0.17
CHA (15.0, 30%)	15.0	0.84	0.30	0.20
CHA (15.0, 44%)	15.0	0.81	0.44	0.16
CHA (26.1, 0%)[b]	26.1	0.97	0.00	0.22

[a] Sample code = CHA (X, Y); X = Si/Al ratio; Y = percentage of Al in 6-MR paired configurations.
[b] Sample at Si/Al = 26 was prepared to assess and eliminate the effects of bulk Al content on kinetic measurements.
[c] Determined by AAS. Uncertainties are ±10%.
[d] Determined by NH_3 TPD. Uncertainties are ±10%.
[e] Fraction of Al in 6-MR pairs determined by Co^{2+} titration (Co and Al quantified by AAS; uncertainties are ±10%).
[f] Calculated from Ar adsorption isotherms (87 K). Uncertainties are ±0.02 cm^3 g^{-1}.

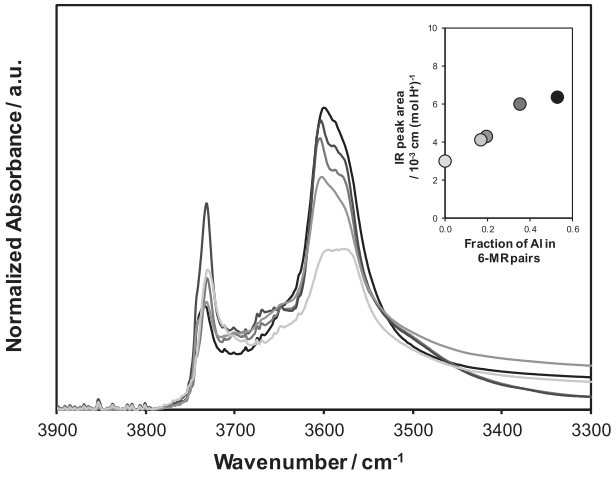

Fig. 1. Normalized IR spectra (415 K) of H-CHA zeolites of fixed Al content with 6-MR paired Al content (CHA (16.0, 0%), CHA (14.8, 18%), CHA (16.2, 24%), CHA (15.0, 30%), and CHA (15.0, 44%)), from light to dark). Inset shows integrated area for the Brønsted OH stretching region as a function of the fraction of Al in 6-MR pairs.

prominent in CHA samples with increasing 6-MR paired Al content (Fig. 1), suggesting that the relative ratios of Brønsted acidic OH groups that give rise to these two features vary systematically with 6-MR paired Al content. Additionally, the integrated area for Brønsted acidic OH stretches increases systematically with the fraction of 6-MR paired Al sites (Fig. 1 inset), even though these samples contain a similar number of framework Al sites (Si/Al = 15) and charge-compensating protons (H^+/Al = 0.75–1.02). Thus, Brønsted acidic OH stretches increase in intensity, on average, with the fraction of 6-MR paired Al sites and associated paired protons (Fig. 1 inset).

IR spectra were collected with increasing temperature (448–748 K) on three H-CHA samples of varying Al arrangement, corresponding to the highest amount of 6-MR paired sites (H-CHA (15.0, 44%), Fig. 2a), an intermediate amount of 6-MR paired sites (H-CHA (14.8, 18%), Fig. 2b), and undetectable amounts of 6-MR paired sites (H-CHA (16.0, 0%), Fig. 2c). For the H-CHA zeolite sample containing predominantly 6-MR isolated Al sites, IR features in the OH stretching region were essentially invariant with temperature (448–748 K, Fig. 2c), and integrated OH peak areas were also independent of temperature (Fig. 2d). In contrast, among H-CHA zeolites containing non-zero percentages of 6-MR paired Al, IR features changed reversibly with temperature (Fig. 2a–b) and integrated OH peak areas decrease systematically with increasing temperature (Fig. 2d). Such reversible decreases in integrated OH absorbance with increasing temperature have been reported previously on FAU, MFI, MOR, and CHA zeolites [46–49], but interpreted to reflect the delocalization of protons from anionic lattice oxygens near framework Al that would cause OH vibrations to disappear altogether [49]. Yet, the temperature insensitivity of OH stretching vibrations in H-CHA zeolites containing predominantly 6-MR isolated Al (Fig. 2c) directly contradicts this interpretation.

Experimental IR spectra reflect ensemble-averaged configurations of protons distributed among the four lattice O atoms associated with each Al site, given that hopping of protons among these O atoms is equilibrated even at ambient temperatures [2,22,50]. Thus, the distribution of OH structures identified in neutron diffraction experiments performed at 5 K [31] are likely very different than those detected in IR spectra at ambient temperatures, and also different still from the distribution of OH sites that prevail at the high temperatures relevant for protolytic alkane cracking reactions (>673 K). As a result, the experimental observations in Figs. 1 and 2 motivate several questions regarding the influence of framework Al proximity on proton configurations in CHA zeolites. First, why do the two IR features in Brønsted acidic OH stretching regions change in relative intensity with Al proximity? Second, why are OH stretching features for protons compensating isolated Al invariant with temperature, while those for protons compensating paired Al sensitive to temperature? Third, why does the integrated OH absorbance (per H^+) increase with Al proximity? To study these questions, we next use DFT methods to identify and characterize Brønsted sites associated with 6-MR isolated and paired Al sites.

3.2. Model assessment of IR spectral features of isolated and proximal protons in CHA

Full details of the CHA structural models used can be found in Fig. S3 (Section S2, SI). Although CHA contains only one crystallographically-unique T-site, charge-compensating protons can be located at four symmetry-distinct lattice O atoms bonded to each Al center. Each O atom is associated with three different rings, which are comprised of 4, 6, or 8 T-atoms. We refer to each unique OH configuration using a three-number code indicating the number of T-atoms in these three rings (644, 844, 864, 884). Fig. 3 shows the local environment of an isolated Al within the CHA framework and the relaxed structures obtained by placing a proton at each of the neighboring O atoms. Calculations show that each unique proton location is associated with a single energy mini-

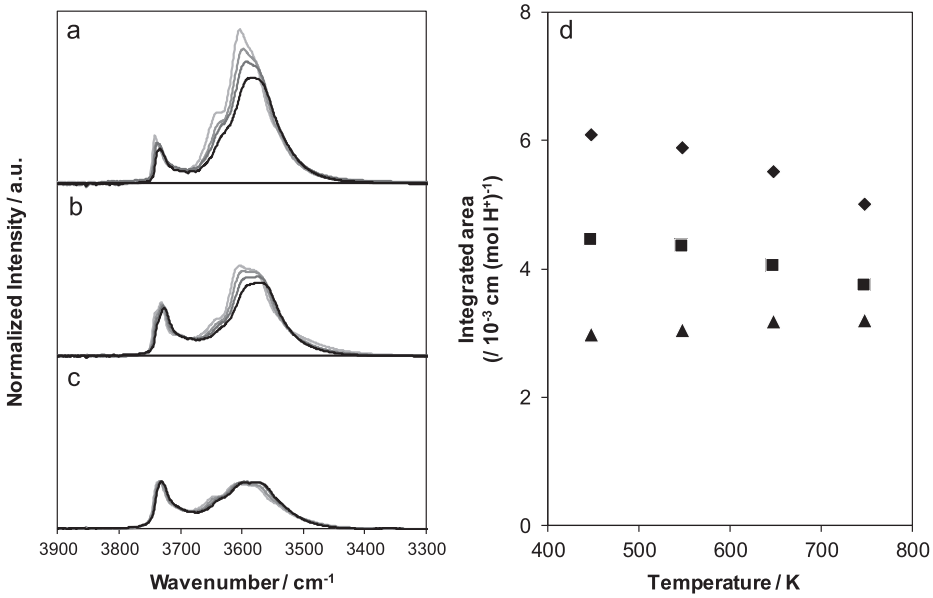

Fig. 2. IR spectra of (a) H-CHA (15.0, 44%), (b) H-CHA (14.8, 18%), and (c) H-CHA (16.0, 0%) as a function of temperature (448 K, 548 K, 648 K, 748 K; light-to-dark). (d) Integrated areas for the OH stretching region on H-CHA (15.0, 44%) (◆), H-CHA (14.8, 18%) (■), and H-CHA (16.0, 0%) (▲) as a function of temperature.

mum, and that in each case the proton is positioned within the largest available ring (either a 6-MR or 8-MR), with similar Al-O-H angles and OH distances among all structures. The four relaxed proton configurations are nearly isoenergetic (within 0.1 eV, Table 2), in quantitative agreement with previous reports for protons located at isolated Al centers in CHA frameworks [22,51].

Using these energies (Table 2) and assuming that the ensemble of proton locations is equilibrated, we computed the Boltzmann-weighted occupancy of the proton at each of these four distinct O atoms as a function of temperature [50,52]. These relative occupancies are plotted in Fig. 4a along with the total number of protons located as part of any 8-MR (calculation details in Section S3, SI). The relative occupancies correspond well with prior predictions based on energies computed in smaller supercells (12 T-sites) [22]. Given that each OH group points into the largest available ring among the three rings it is contained within, macroscopically observed differences in proton siting between 6-MR and 8-MR locations reflect the identity of the O atom associated with the proton and not the occupation of different rings by a proton at a given O atom. The relative populations of the four proton configurations vary less than 10% across the temperature range studied (448–748 K). Moreover, the total number of protons pointing into an 8-MR is nearly constant within this temperature range, because the decrease in the population of lower-energy 844 sites is compensated by an increase in the population of higher energy 884 sites. Similar evaluations computed within a smaller supercell (12 T-sites) also provided relative energies within 10 kJ mol^{-1}, and proton occupancies that varied by ~20% over a similar temperature range (300–800 K) [22].

We computed harmonic vibrational frequencies and intensities via oscillator strengths of each configuration to determine IR peak centers and intensities, respectively (computational details in Section S3, SI). Harmonic vibrational frequencies ranged from 3681 to 3707 cm^{-1} and systematically overestimated experimental observation (Table S1, SI). To facilitate comparison with experiment, we compared the observed peak center of the high frequency feature (3606 cm^{-1}) to the highest frequency simulated mode to obtain a scaling factor of 0.973, and applied this factor to all simulated modes. Calculated and adjusted vibrational modes are listed in Table S1 (Section S3, SI). Simulated IR spectra were constructed (procedures outlined in Section S3, SI), as shown in Fig. 5 for a proton at each of the four O sites, and the composite spectrum obtained from the summation of their Boltzmann-weighted contributions at 448 K. The resulting spectra have two distinct features separated by 24 cm^{-1}, in agreement with previous IR simulations [22] and experimental data [46] for H-CHA zeolites (Fig. 2). The vibrational feature at ~3600 cm^{-1} predominantly reflects protons at the O site at the edge of the double six-membered ring (844, Fig. 3c), while the feature at ~3580 cm^{-1} reflects contributions from protons at the other three O sites (644, 864, 884) that correspond to proton locations in both 6-MR and 8-MR environments. This observation calls into question previous assignments of features at 3600 cm^{-1} and 3575 cm^{-1} to protons residing in 8-MR and 6-MR environments of CHA, respectively, inferred from neutron diffraction data collected at 5 K [31].

The composite spectrum generated by adding the four principal component features for each O site results in two IR peak centers at ~3600 and ~3580 cm^{-1} with approximately equal intensity, similar to that observed in experimental IR spectra of protons in H-CHA zeolites containing isolated Al sites (Fig. 2c). Additionally, because the population of protons among the four O sites differ by less than 10% from 448 to 748 K (Fig. 4a), simulated IR spectra only exhibit variations with temperature that arise from slight shifts away from the 844 site (Fig. 6a), even though the principal components for each OH group has a distinct vibrational frequency and oscillator strength. Therefore, we conclude that experimental IR spectra of protons compensating isolated Al in H-CHA zeolites (Fig. 2c) are insensitive to temperature because the equilibrium distribution of protons among O sites has a weak dependence on temperature.

We next compare protons that charge-compensate paired Al arrangements. ^{29}Si MAS NMR data suggest that second nearest neighbor (Al-O-Si-O-Al) configurations are uncommon in CHA zeolites (Si/Al ~ 15) synthesized with mixtures of TMAda$^+$ and Na$^+$ [20]. Therefore, we considered three different types of Al-Al site pairs, including fourth-nearest-neighbor (4NN) in an 8-MR, 3NN in an 8-MR, and 3NN in a 6-MR. Fig. 7 shows these three Al-Al site pair configurations along with labels identifying the four framework oxygen atoms associated with each Al. Thus, a given Al-Al site pair has up to 16 distinct configurations arising from protonation of one of each set of four framework oxygen. Symmetry consider-

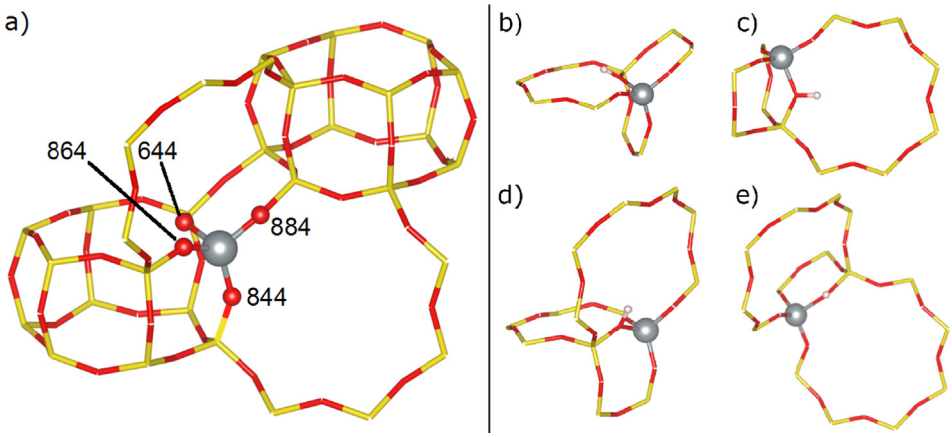

Fig. 3. (a) Local environment of an isolated Al center and its four symmetry-distinct proximal O atoms in the CHA framework. Energy-minimized locations of protons at the (b) 644, (c) 844, (d) 864, and (e) 884 O atoms. Red and yellow nodes correspond to Si and O, respectively; gray and white spheres correspond to Al and H, respectively.

Table 2
GGA computed relative energies, scaled harmonic vibrational frequencies, and infrared intensities of OH sites at isolated Al atoms.

Proton Location	Relative Energy/ eV	OH Frequency/ cm^{-1}	OH IR Intensity/ $(eÅ)^2$
644	0.030	3581	0.192
844	0.000	3606	0.217
864	0.023	3583	0.230
884	0.065	3589	0.189

ations reduce this number to 10 for 4NN in an 8-MR and 3NN in a 6-MR.

We constructed each proton configuration for each Al-Al site pair, and then relaxed their structures. As with the isolated proton case, the charge compensating protons always point into the largest available void, either an 8-MR or 6-MR. Local proton structures are generally convolutions of the isolated proton structures shown in Fig. 3b–d when protons occupy different rings. When protons occupy the same ring, including the 884–864 and 884–884 combinations of the 4NN 8-MR Al site pair, the 864–844, 864–884, 884–884, and 884–844 combinations of the 3NN 8-MR Al site pair, and the 644–644 combination of the 3NN 6-MR Al site pair (Fig. 7a–c), proton locations are more significantly perturbed out of the ring plane and Al are distorted further from their ideal locations. As noted below, such configurations that require protons to occupy the same ring are always the highest energy members of the configurational set.

The relative energies of each set of proton configurations for the three Al-Al site pairs are reported in Fig. 8, ordered according to decreasing physical distance between the two Al sites going from Fig. 8a–c. Energies are referenced to the lowest energy member of each Al-Al site pair ensemble. At the largest Al-Al separation (Fig. 8a), the highest-energy configurations always contain at least one 884 proton (as in the case for an isolated Al, Table 2), with the 884–884 combination of two protons in the same 8-MR being the highest in energy. The 844, 864, and 644 protons, all of which are similar in energy in the isolated case (Table 2), form an ensemble of seven symmetry-distinct pairs, all of which are similar in energy in the paired case. Interactions at this distance are non-zero, however, as evidenced by the low energy of the 884–844 combination. In the 3NN 8-MR case (Fig. 8b), proton-proton interactions become more pronounced, as evidenced by the larger span in relative energies. The 844–864 configuration, which places two protons in the same 8MR, is highest in energy. Structures that place one proton at either the 864 or 844 locations within the 8-MR and the remaining proton outside this ring are lowest in energy, reflecting favorable interactions across the siloxane ring between the intra-ring proton and Lewis basic framework O associated with the Al.

The ten unique 3NN 6-MR paired proton configurations span ~0.4 eV in relative energy (Fig. 8c), in agreement with previous reports [51]. The 644 proton is a member of the lowest and highest energy configurations. As shown in Fig. 7c, the high energy 644–644 combination places two protons in exact opposition and close proximity within the same ring; in contrast, the three remaining combinations, which are nearly isoenergetic, maximize separation

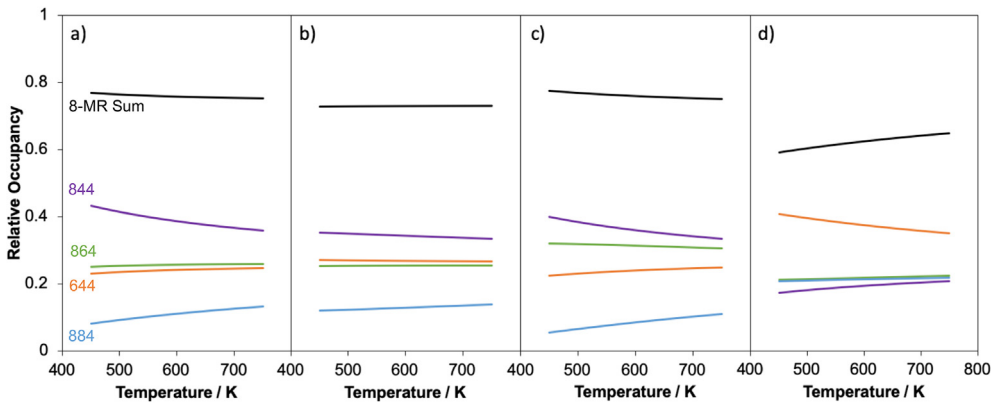

Fig. 4. Relative occupancy of protons at crystallographically-distinct O atoms at a) isolated Al atom, b) 4NN pair: 8-MR, c) 3NN pair: 8-MR, and d) 3NN pair: 6-MR in CHA. 644 (orange), 844 (purple), 864 (green), 884 (light blue), and sum of 844, 864, and 884 configurations (black).

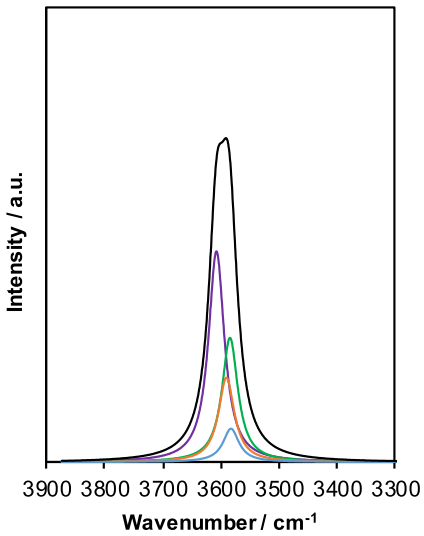

Fig. 5. Simulated IR spectra for protons at O atoms in CHA at 448 K. 644 (orange), 844 (purple), 864 (green), 884 (light blue), and summation of these contributions (black). Intensities are scaled to the most intense feature across all proton configurations, for ease of visualization.

between the two protons while allowing the 644 proton to relax towards the 644 oxygen associated with the second Al site. Fig. 9 compares the local structures of the 644 proton with and without an Al at the 3NN position in the 6-MR. When a second Al is present, the OH bond length is unchanged but the 6-MR ring puckers to decrease the cross-ring OH distance by 0.5 Å (Fig. 9b).

Using the energies in Fig. 8, the relative occupancy of protons at the four distinct O atoms in the CHA framework for each of the three Al-Al site pair types were calculated as a function of temperature by a Boltzmann-weighted average and are shown in Fig. 4b–d. The relative populations in both 8-MR pair cases (3NN and 4NN 8-MR) are similar to the isolated case, with the proton sites populated in the same order (Fig. 4b and c) and remaining approximately constant with temperature. In contrast, the relative ring populations in the 3NN 6-MR case differ substantially from the isolated case and vary with temperature (Fig. 4d). 6-MR proximal Al atoms perturb the proton arrangements relative to an isolated Al site or to an Al located in 3NN or 4NN 8-MR site pairs, as evidenced by the larger fraction of protons that occupy the 644 O site at 6-MR paired than in isolated configurations (~40% and ~20%, respectively).

We computed the vibrational spectra of all possible convolutions of the proton locations shown in Fig. 7 for each Al-Al site pair type (results in Figs. S5–S7, SI). All spectra contain two features corresponding to the two proton environments, with vertical lines denoting the corresponding isolated proton frequencies. In 8-MR Al-Al site pairs (Figs. S5 and S6, SI), spectra are generally combinations of the isolated proton results. In the 3NN 6-MR Al-Al site pair (Fig. S7, SI), vibrational modes couple more strongly in many cases and are thus split. In the cases in which a proton is sited at the 644 oxygen (three lowest energy configurations in Fig. 7c), the vibrational frequency associated with that proton is shifted further from that of an isolated 644 proton, reflecting the cross-ring interactions illustrated in Fig. 9b.

Vibrational intensities were computed from oscillator strengths (Eq. (S2), SI) and are plotted as a function of relative energy for the 4NN and 3NN 8-MR configurations in Fig. S4a and S4b (SI), along with the predicted intensities for the isolated Al case for comparison (each paired configuration contributes two distinct intensities corresponding to the two O-H modes in the supercell). Computed vibrational intensities for these paired proton configurations are generally indistinguishable from those for isolated protons, and are generally independent of relative energy of the configuration (Fig. S4, SI). We used a Boltzmann weighting of the individual spectra to generate the simulated composite IR spectra for the isolated Al case and all three Al-Al site pair types as a function of temperature (448–748 K) shown in Fig. 6b and c (normalized per H^+ for comparison with the isolated case). The simulated IR spectra of the two 8-MR Al-Al site pairs contain a single, temperature-independent feature at ~3590 cm^{-1} (Fig. 6b and c). This feature arises from the convolution of protons in 8-MR and 6-MR voids with similar relative energies and oscillator strengths (as shown in Fig. S4a and S4b, SI). The frequency for the lowest energy configurations varies from 3574 to 3616 cm^{-1}, and the Boltzmann weighted average frequency is 3593 cm^{-1} for the 3NN 8-MR pair and 3592 cm^{-1} for the 4NN 8-MR pair. This single IR feature is in the range of the isolated proton IR signature; thus, protons compensating 8-MR Al-Al site pairs appear to be spectroscopically indistinguishable from those compensating an isolated Al site.

In contrast, for the 3NN 6-MR case (Fig. S4c, SI), several low energy proton configurations have computed intensities significantly greater than the isolated (or the 8-MR paired proton) modes. The simulated IR spectra of the 3NN Al-Al site pair in the 6-MR (Fig. 6d) contains two features separated by ~20 cm^{-1}, similar in origin to the isolated proton spectrum. However, the high frequency feature in the 3NN 6-MR spectrum (3567 cm^{-1}) is more intense than the low frequency feature (3546 cm^{-1}), in agreement with observed IR spectra for samples containing non-zero fractions of 6-MR paired Al sites (Fig. 2b and c). This high frequency feature is attributed to protons on the 884 and 864 oxygen in the lowest energy configurations, while the low frequency feature is attributed to the protons on the 644 oxygen in those same configurations. The higher intensities result in larger integrated areas in the simulated spectrum in Fig. 6d. Further, because higher energy configurations have lower intensities (Fig. S4c, SI), the integrated intensity of 3NN 6-MR proton ensembles decreases with increasing temperature (Fig. 6d). These results are qualitatively consistent with the trends observed in experimental spectra shown in Fig. 2b and c for H-CHA zeolites with 18% and 44% of Al in 6-MR paired configurations. The model results assume that broadening is temperature-independent, that proton spectra can be decomposed uniquely into contributions from isolated and paired sites, and that normalization of intensities to Al content captures the experimental (potentially temperature-dependent) normalization. Thus, quantitative comparisons between observation and model are not possible. Rather, models provide insight and rationalization of one factor that influences observation.

Based on the body of experimental and computational results, we conclude that the observed temperature dependence in the IR spectra of CHA samples containing 6-MR paired Al sites can only be rationalized by the population of 3NN Al-Al site pairs in the 6-MR. Vibrational spectra of 3NN and 4NN Al pairs in an 8-MR are expected to be temperature-independent and to occupy the same spectral region as isolated protons. Proton distributions among the four O atoms in $[AlO_2]^-$ tetrahedra depend on the local arrangement of Al in lattice positions, because the relative energies of proton sites depend on their void environment and proton-proton proximity [53]. The energetic biasing of certain proton configurations imparted by 6-MR paired Al arrangements in CHA results in experimentally observed OH vibrational features that are sensitive to temperature, because each proton site differs in its oscillator strength and thus has a different intrinsic peak intensity.

3.3. Distribution of protons in partially Na-exchanged CHA zeolites

The partial replacement of H^+ with Na^+ has been reported to influence the molar absorptivity and temperature dependence of

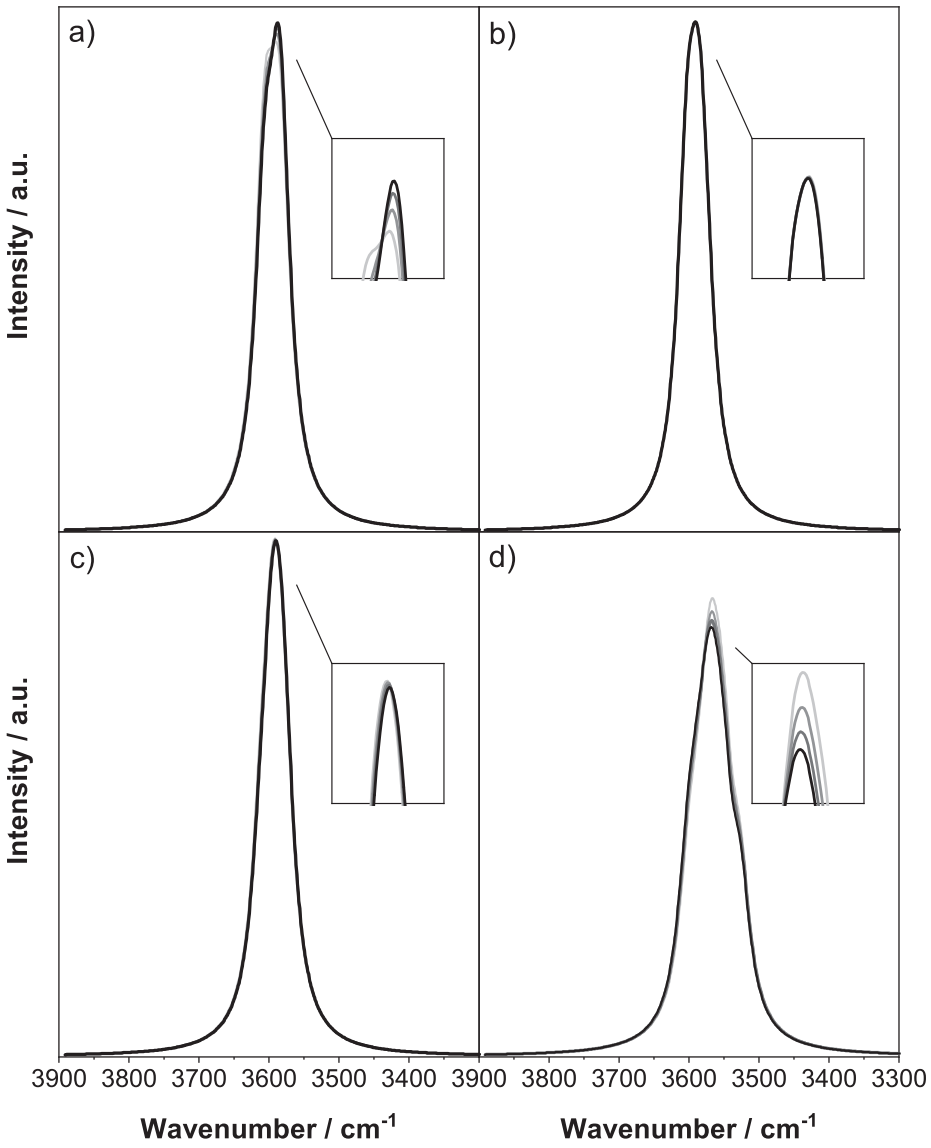

Fig. 6. Simulated temperature-dependent IR spectra of protons at a) isolated Al, b) 4NN pair: 8-MR, c) 3NN pair: 8-MR, and d) 3NN pair: 6-MR in CHA. Temperatures range from 448 K (light) to 748 K (dark) in 100 K increments. Insets show magnified views of peak maxima. Intensities are scaled to the most intense feature across all proton configurations, for ease of visualization.

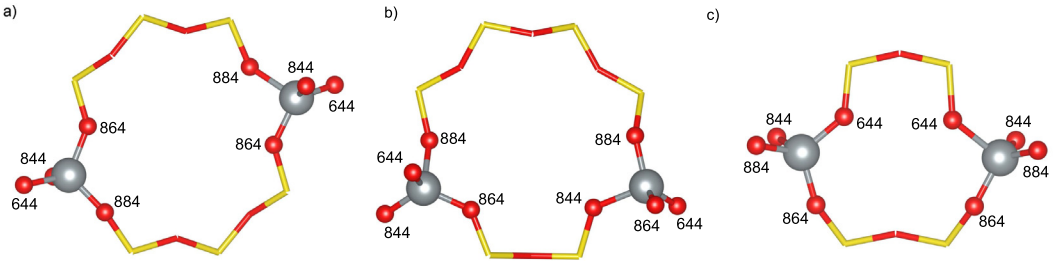

Fig. 7. Spatial relationship between Al pairs and associated framework oxygen in a) 4NN Al pair in an 8-MR, b) 3NN Al pair in an 8-MR, and 3NN Al pair in a 6-MR. Numerical labels framework oxygen ring occupancy. Structures drawn are extracted from lowest energy proton-compensated structures. Red and yellow nodes correspond to Si and O, respectively; gray and white spheres correspond to Al and H, respectively.

the residual OH stretches in IR spectra of FAU zeolites. In certain cases, residual OH stretches are insensitive to temperature (Na^+/Al = 0.83, Si/Al = 1.3, T = 298–673 K) [47], suggesting that Na^+ may preferentially titrate 6-MR paired Al arrangements to leave behind residual protons that compensate Al with 3NN (or greater) separation in larger rings. Here, we study these phenomena by partial Na^+ titration of protons in CHA samples containing various amounts of 6-MR isolated and paired Al sites; the names of these samples contain a "Na_xH_y" prefix where *x* and *y* refer to the percentage of exchange sites occupied by that cation. The number of

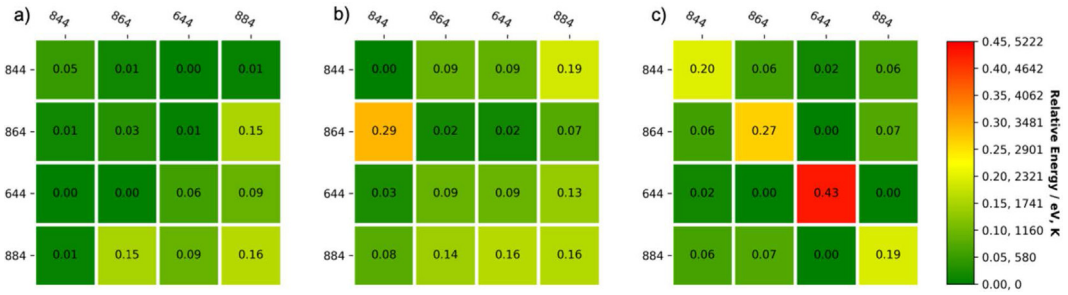

Fig. 8. Relative proton configuration energies (shown as a heat map) and characteristic temperature, for a) 4NN 8-MR, b) 3NN 8-MR, and c) 3NN 6-MR Al-Al site pairs in CHA; rows and columns represent locations of the two protons. In the 3NN 8-MR case, rows and columns refer to the left and right Al in Fig. 7b respectively.

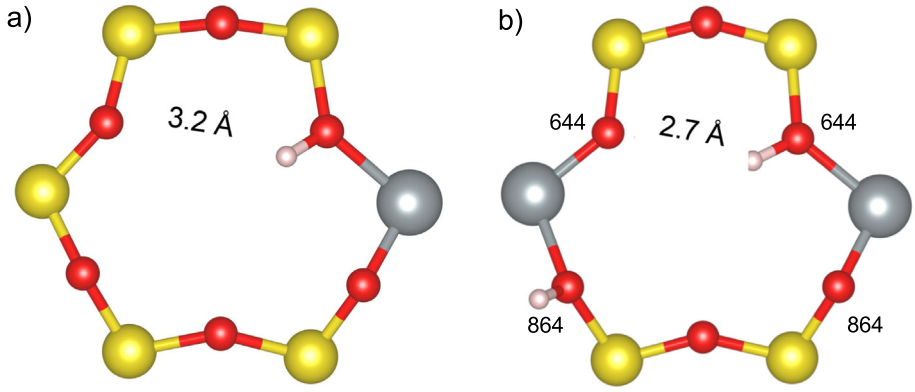

Fig. 9. Images of the 6-MR extracted from relaxed supercells of a 644 proton associated with a) an isolated Al, and b) the 864–644 6-MR paired Al configuration.

residual protons after Na-exchange was quantified by NH_3 TPD and shown in Table 3. Fig. 10a and b show observed IR spectra of CHA zeolites with 18% and 44% Al in 6-MR pairs, respectively, and ~50% of their protons exchanged with Na^+ cations. Normalized absorptivity in the OH stretching region decreased reversibly with increasing temperature (448–748 K), as observed in H-CHA zeolites containing a non-zero fraction of 6-MR Al pairs (Fig. 2a and b).

The change in the observed IR spectra after Na^+ exchange motivates two questions. First, does a sodium cation prefer to titrate isolated Al (including 3NN and 4NN 8-MR) or 6-MR paired Al configurations? Second, how does Na^+ exchange influence the residual proton distributions, and thus residual OH IR stretching features? We used the supercell DFT model to establish the siting preference of an isolated Na^+ (ZNa). Unlike a proton, the data show that Na^+ prefers to coordinate near two framework O associated with an Al. The tetrahedron centered by an Al has six such possible locations. The three locations that place Na^+ within a 4-MR are computed to be unstable. Of the remaining three possibilities, placement of Na^+ within the 6-MR (Fig. 11a) is preferred over either 8-MR location by about 0.1 eV.

We next considered co-incorporation of a proton and Na^+ cation at a 3NN 6MR Al-Al site pair, after doubling the size of the supercell along the *b* lattice vector to 72 T-sites to avoid periodic image artifacts. We considered all combinations of the three Na^+ locations with four proton locations, Z_2HNa (Section S5, SI). As with the isolated proton case, the proton always relaxes into the largest available void. Relative energies of the twelve resulting configurations are reported in Fig. 12. Energies of these twelve configurations span a range of ~0.5 eV, similar to the range observed for H^+-H^+ pairs. Of these twelve configurations, the three lowest in energy contain the Na^+ cation in the 6-MR (as shown in Fig. 11a), leaving the proton to reside in an 8-MR and suggesting that the larger Na^+ cations preferentially occupy smaller voids in CHA zeolites. Further, the Na^+ cation excludes H^+ from the same void: the configuration in which both the Na^+ and H^+ nominally occupy the same 6-MR is highest in energy of the 12 combinations, and the proton is displaced substantially out of the ring plane. Distinctly low in energy is a configuration that places Na^+ within a 6-MR void and places the proton on the 844 site (Fig. 11c). This arrangement is a combination of the lowest energy isolated Na^+ and isolated H^+ locations.

Table 3
Residual proton content in Na-H-CHA zeolites, relative to H-form samples.

Zeolite	H^+/H^+_{parent} [a]
$Na_{47}H_{53}CHA$ (14.5, 0%)	0.53
$Na_{59}H_{41}CHA$ (14.5, 0%)	0.41
$Na_{49}H_{51}CHA$ (14.8, 18%)	0.51
$Na_{36}H_{64}CHA$ (15.0, 44%)	0.64
$Na_{55}H_{45}CHA$ (15.0, 44%)	0.45
$Na_{69}H_{31}CHA$ (15.0, 44%)	0.31

[a] Measured by NH_3 TPD. Errors are ±10%.

To confirm that 3NN 6-MR Al pair sites preferentially exchange only one of the H^+ sites with Na^+, we also computed structures and energies of two Na^+ cations compensating a 6-MR paired Al site. One Na^+ occupies the 6-MR void, while the second prefers to occupy the 8-MR bound to the 844 and 864 oxygens (details in Section S5, SI). Taking the lowest energy isolated configurations as references, we can determine the site preferences of a Na^+ ion from the energies of the two exchange reactions (details in SI Section S5):

$$ZNa + Z_2H_2 \rightarrow ZH + Z_2HNa \quad (1)$$

$$ZNa + Z_2HNa \rightarrow ZH + Z_2Na_2 \quad (2)$$

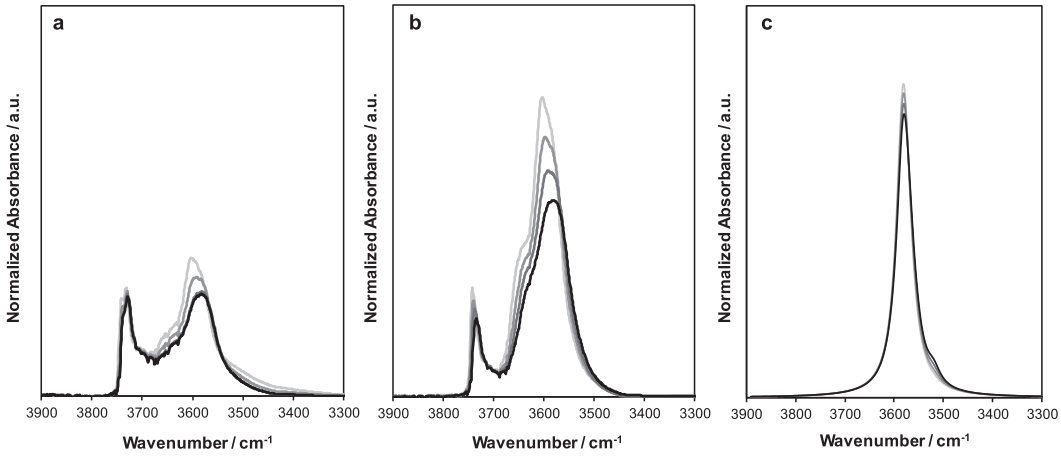

Fig. 10. Normalized IR spectra of Na-H-CHA zeolites at 448 to 748 K in 100 K intervals from light to dark. (a) $Na_{49}H_{51}CHA$ (14.8, 18%); (b) $Na_{55}H_{45}CHA$ (15.0, 44%), (c) simulated Na-H-CHA IR. Simulated intensities are scaled to the most intense feature across all proton configurations, for ease of visualization.

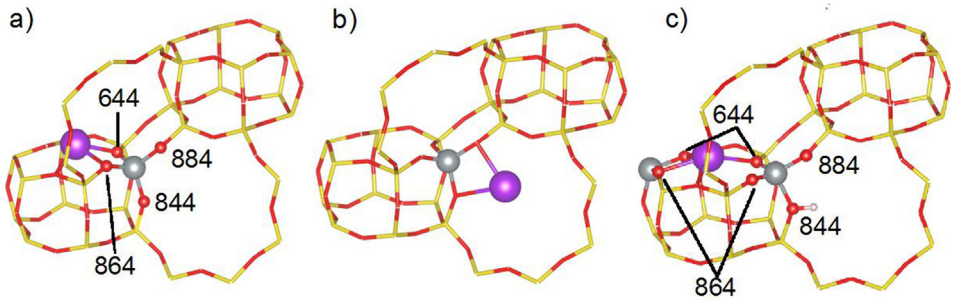

Fig. 11. Isolated Al site charge-compensated by Na^+ in the (a) 6-MR and (b) in one of the two 8-MR voids. (c) Energy-minimizing configuration of a 3NN 6-MR paired Al site compensated by an Na^+ and proton.

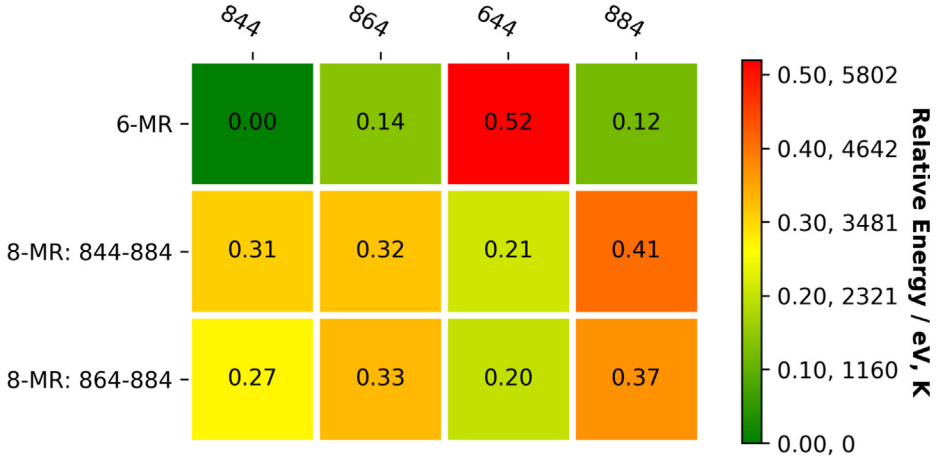

Fig. 12. Relative energies, and characteristic temperature, for the 12 unique Na^+-H^+ configurations at paired Al sites. Rows represent location of Na^+ and columns represent location of H^+.

The computed energies of these two reactions are −0.11 and +0.10 eV, respectively, consistent with selective titration of 6-MR paired Al sites with a single Na^+ cation, followed by Na^+ titration of isolated Al sites.

We computed the vibrational spectra of all the Z_2HNa combinations of Fig. 12 (details in Section S5 and Fig. S9, SI) and calculated the Boltzmann-weighted average to obtain the composite synthetic spectrum shown in Fig. 10c. From Fig. 12, the 844 proton is the primary contributor to the IR spectrum, and the proximal Na^+ is computed to shift its frequency down to 3580 cm^{-1} from the 3606 cm^{-1} of an isolated 844 proton. With increasing temperature, the 884 proton increasingly contributes to the composite spectrum. While the 884 OH stretching frequency (~3570 cm^{-1}) is similar to that of 844, its intrinsic intensity is lower, resulting in a decrease in the overall intensity of the IR feature with increasing temperature. These results are able to reproduce the temperature-sensitivity of the Na^+-titrated sites observed experimentally in Fig. 10a and b. Thus, a proton adjacent to Na^+ in a 6-

MR is expected to exhibit temperature sensitivity as in the case of a paired proton in a 6-MR, instead of the temperature insensitivity of an isolated proton.

3.4. Kinetic assessments of isolated and paired protons in CHA zeolites using protolytic propane cracking

We use protolytic propane cracking as an acid-catalyzed probe reaction because it occurs at conditions wherein protons remain uncovered during catalysis [5,54], reflecting the conditions studied by IR spectroscopy and DFT. The mechanism of protolytic propane cracking proceeds via a protonation of a C-C bond to form a three-center, two-electron $(C\text{-}C\text{-}H)^+$ carbonium ion-like transition state that decomposes to form methane and ethene [55–57] (additional discussion in Section S.6, SI). Propane cracking rates (per H^+, 718–778 K) increased linearly with propane pressure (Fig. S10, SI), apparent first-order cracking rate constants were independent of propane site-contact time (Fig. S11, SI), ethene and methane were formed in equimolar quantities (1.0 ± 0.10), and products larger than C_3 were not observed; all of these observations are consistent with the sole involvement of the protolytic mechanism for propane activation at the conditions studied here [55]. We note that protolytic propane dehydrogenation to form propene and H_2 also occurs in parallel with cracking reactions on H-zeolites; however, we have recently shown that steady-state propene formation rates measured on H-zeolites also include contributions from hydrogen transfer reactions with dehydrogenated forms of surface carbonaceous deposits that form *in situ* within H_2-deficient regions of catalyst beds [58]. Rigorous measurements of protolytic dehydrogenation rates at Brønsted acid sites require extrapolating rate data to initial time-on-stream with H_2 co-feeds, which suppress the formation and reactivity of carbonaceous deposits; given that such H_2 co-feeding experiments were not performed in this study, we have not reported or discussed propane dehydrogenation rates here. Propane cracking rates measured in the absence of co-fed H_2 can be ascribed solely to the presence and function of Brønsted acid sites, however, because any reaction-derived carbonaceous active sites that may form during reaction are unable to convert propane into methane or ethene in detectable quantities under conditions wherein protolytic mechanisms of alkane activation prevail [58].

Table 4 shows apparent first-order propane cracking rate constants (per H^+, 748 K) on H-CHA samples with different percentages of Al in 6-MR paired configurations, along with apparent activation energies and entropies calculated from the temperature dependence of these rates (additional discussion in Section S.6, SI). Four distinct H-CHA samples that contain predominantly 6-MR isolated Al sites at different bulk Al density (Si/Al = 15–26) showed similar first-order rate constants for propane cracking ($k_{app,iso}$ = 0.4 × 10^{-3} mol (mol H^+)$^{-1}$ s^{-1} (bar C_3H_8)$^{-1}$, Table 4), providing evidence that both a similar distribution of H^+ sites exist among these samples and that measured rates are uncorrupted by intracrystalline transport phenomena, as expected from previous reports of protolytic propane activation [5]. First-order propane cracking rate constants, normalized by the number of total H^+ sites, differ by ~8× among H-CHA samples of varying Al arrangement (Table 4). These data indicate that protons are not equally reactive, despite the single T-site available for Al substitution in CHA zeolites and the similar bulk composition (Si/Al ~ 15) of the samples studied.

Propane cracking rate constants (per H^+, 748 K) increased monotonically with the fraction of Al in 6-MR pairs (Fig. 13). Assuming that isolated and 6-MR paired Al sites behave as two independent site ensembles, measured propane cracking rates can be described using a weighted-average of the kinetic contributions of each site type, allowing the apparent rate constant on any sample to be described by:

Table 4
Monomolecular propane cracking rate constants (748 K, per H^+), apparent activation energies, and apparent activation entropies on H-CHA zeolites.

Sample	k_{app}[a]/10^{-3} mol (mol H^+)$^{-1}$ s^{-1} (bar C_3H_8)$^{-1}$	E_{app}[b]/kJ mol^{-1}	ΔS_{app}[c]/J mol^{-1} K^{-1}
H-CHA (14.5, 0%)	0.4	164	−99
H-CHA (16.0, 0%)	0.3	159	−106
H-CHA (17.5, 0%)	0.4	156	−110
H-CHA (15.5, 8%)	1.0	167	−86
H-CHA (15.5, 13%)	0.8	153	−107
H-CHA (14.8, 18%)	1.1	159	−97
H-CHA (13.8, 20%)	1.7	171	−77
H-CHA (16.2, 24%)	1.2	169	−82
H-CHA (15.0, 44%)	2.5	166	−80
H-CHA (26.1, 0%)	0.3	154	−114
H^+_{iso}[d]	0.4	163	−105
H^+_{pair}[d]	5.1	163	−79

[a] Uncertainty is ±15%.
[b] Uncertainty is ±8 kJ mol^{-1}.
[c] Uncertainty is ±9 J mol^{-1} K^{-1}.
[d] Determined from linear fit (Eq. (5)) to 0% and 100% 6-MR Al pairs (Fig. 13).

$$k_{app} = k_{app,iso}X_{iso} + k_{app,pair}X_{pair} \quad (3)$$

In Equation (3), X_{iso} and X_{pair} are the fraction of Al sites in isolated and 6-MR paired configurations, respectively; $k_{app,iso}$ and $k_{app,pair}$ are their respective first-order propane cracking rate constants. This model is represented by the solid line in Fig. 13, and the estimated apparent rate constant for monomolecular propane cracking at paired protons is 5.1 × 10^{-3} mol (mol H^+)$^{-1}$ s^{-1} (bar C_3H_8)$^{-1}$, which is ~12× higher than that for cracking at isolated protons.

Apparent activation energies for propane cracking were similar on all H-CHA zeolites (153–171 kJ mol^{-1}, Table 4) and did not vary systematically with the number of 6-MR paired Al sites (Fig. S12a, SI). As a result, values for the apparent activation energy estimated for propane cracking at isolated and paired proton sites were similar (163 kJ mol^{-1}, Table 4). These activation energies are similar to those reported for H-CHA (164 kJ mol^{-1} by Kester et al. [58], 170–179 kJ mol^{-1} by Yun et al. [59]), and in the range of values reported for H-form zeolites of varying topology (Fig. S12a, SI). DFT estimates of deprotonation energies (DPE) indicate that protons compensating 6-MR Al-Al site pairs in CHA can behave as stronger acids (lower DPE values by >10 kJ mol^{-1}) than isolated protons, because a deprotonated AlO_2^- tetrahedron can be stabilized by hydrogen bonding with a spectating proton across the 6-MR (as shown in Fig. 9b) [53]; however, a similar energetic benefit is captured upon stabilizing the late carbonium-ion pair transition states (+0.9e [60–63]) so as to attenuate the influence of DPE changes on [5] apparent activation energy values (additional discussion and interpretation using Born-Haber thermochemical cycles discussed in Section S.6, SI).

Apparent activation entropies for propane cracking became systematically less negative with increasing fractions of Al in 6-MR paired configurations (Fig. S12b, SI), and were ~25 J mol^{-1} K^{-1} less negative at 6-MR proton pairs (−79 J mol^{-1} K^{-1}, Table 4) than isolated protons (−105 J mol^{-1} K^{-1}, Table 4). The systematic increase in apparent activation entropies, despite similar apparent activation energies, with increasing 6-MR paired site content is thus responsible for the 12× higher first-order propane cracking rate constants for paired than isolated sites (Fig. 13, Table 4). The less negative apparent activation entropy at proximal proton sites has been proposed previously (in MFI) to reflect carbonium ion-like transition states that were more product-like and occurred later along their reaction coordinates than at isolated protons [14], which would appear to allow capturing a larger fraction of the entropic gains associated with the hindered rotations and rocking vibrations that are accessed upon carbon–carbon bond cleavage [64] (additional discussion in Section S.6, SI).

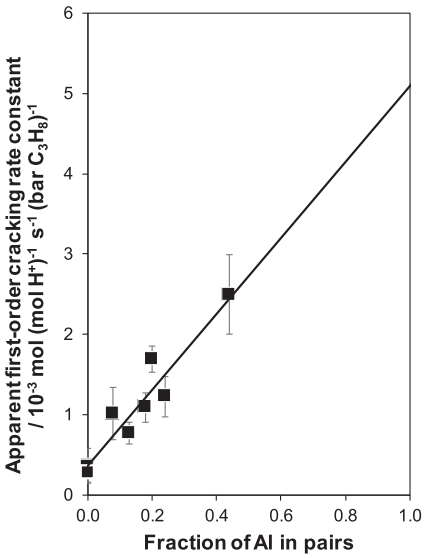

Fig. 13. Apparent first-order propane cracking rate constants (748 K, per H^+) on H-CHA zeolites plotted as a function of the fraction of Al in 6-MR pairs. Solid line represents least-squares regression of the data to Eq. (3).

Heterogeneities in Brønsted acid site reactivity can be identified by titration or poisoning experiments, given a titrant (e.g., Na^+) that preferentially removes sites of different reactivity; for example, Na^+ preferentially exchanges protons in smaller 8-MR side pockets than in 12-MR channels of MOR zeolites, with the former confining the more reactive proton sites for dimethyl ether carbonylation [4] and protolytic alkane activation [5]. Here, NH_4-CHA samples containing either 0% or 44% of Al in 6-MR pair configurations were partially exchanged with Na^+, and the number of residual protons was quantified by NH_3 TPD. The names of these samples contain a "Na_xH_y" prefix where x and y refer to the percentage of exchange sites occupied by that cation, and are listed in Table 5 along with measured first-order propane cracking rate constants (748 K, per residual H^+), and apparent activation energies and entropies.

Propane cracking rate constants (748 K, per initial H^+) on Na-H-CHA zeolites are shown in Fig. 14 as a function of Na^+ content. Rate constants on Na-H-CHA (14.5, 0%), normalized by initial H^+ content, decreased linearly as H^+ sites were titrated by Na^+ to increasing extents (Fig. 14 inset); thus, rate constants (per residual H^+) remained similar as H^+ sites were replaced with Na^+ (0.3–0.4 × 10^{-3} mol (mol residual H^+)$^{-1}$ s^{-1} (bar C_3H_8)$^{-1}$, Table 5). Apparent activation energies and entropies also did not vary systematically with decreasing H^+ density (Table 5), suggesting that the distribution of residual proton sites in Na-H-CHA zeolites containing isolated framework Al centers was unaffected by the presence of Na^+. This provides further evidence that isolated protons in CHA are equivalently reactive for protolytic propane cracking, the behavior expected of a quintessential single-site catalyst [65], consistent with the similar first-order rate constants among H-CHA samples of different bulk Si/Al ratio but prepared to contain predominantly isolated Al sites (Table 4).

In sharp contrast, as H^+ sites on Na-H-CHA (15.0, 44%) were titrated by Na^+ to increasing extents, propane cracking rate constants (normalized by initial H^+ content) decreased faster than expected from the equimolar titration of sites of equivalent reactivity (Fig. 14); thus, propane cracking rate constants (per residual H^+) on Na-H-CHA (15.0, 44%) decreased systematically from 2.5 to 0.3 (×10^{-3} mol (mol residual H^+)$^{-1}$ s^{-1} (bar C_3H_8)$^{-1}$, Table 5) with increasing extents of H^+ site replacement with Na^+. Apparent activation energies were similar on this series of Na-H-CHA zeolites (162–166 kJ mol^{-1}, Table 5), while apparent activation entropies became ~20 J mol^{-1} K^{-1} more negative (−80 to −99 J mol^{-1} K^{-1} Table 5) with increasing Na^+ titration. Propane cracking rates, activation energies, and activation entropies measured on the $Na_{69}H_{31}$CHA (15.0, 44%) sample were similar to those on H-CHA zeolites containing predominantly isolated Al (such as the Na_0H_{100}CHA (14.5, 0%) sample, Table 5). These kinetic data provide evidence that a similar distribution of proton sites is present on these two samples, and thus that Na^+ preferentially titrates 6-MR Al pairs such that the residual H^+ protons are predominantly isolated. These findings are consistent with the preferential titration 6-MR paired Al sites in CHA by Na^+ as identified by DFT (Section 3.3, Equation (1)), and further suggest that the resulting proton-sodium site pairs formed at a 6-MR paired Al configuration behave catalytically similar to a proton at an isolated Al site. These data also suggest that the entropic stabilization of carbonium ion-like transition states conferred by a proximal spectating proton is not conferred by a proximal Na^+ cation.

3.5. Implications of proton proximity for interpreting IR spectra and alkane cracking reactivity in non-CHA zeolites

Reversible decreases in molar absorptivity in the OH stretching IR region with increasing temperature (373–773 K) have been observed on FAU, MOR, MFI, and CHA zeolites [46–49], and collectively attributed to the deprotonation of Brønsted acid protons from the lattice at high temperatures. These observations stand in stark contrast with those of isolated protons in CHA, whose IR spectra are insensitive to temperature (Fig. 2c and 6a). As shown here, changes in proton populations at 6-MR paired Al configurations in CHA vary with temperature and cause concomitant changes in IR spectral features and intensities. OH IR spectra for MFI have been shown to be sensitive to temperature, even in the dilute Al limit (Si/Al = 35–90) [49]. The greater temperature sensitivity of OH IR spectra of MFI zeolites could reflect a greater sensitivity of proton siting to temperature than in the case of CHA. To test this hypothesis, we used previously reported, DFT-computed relative proton site energies at symmetry-distinct and isolated Al in MFI, Beta, MOR, FER, CHA, and FAU [52] to compute the Boltzmann probability of the lowest energy proton site at 448 and 748 K, using the same assumptions (Eq. (S1), SI) that underlies Fig. 4. The difference between these two probabilities (P1(448 K)–P1(748 K)) represents the expected decrease in population of that lowest energy proton between 448 and 748 K. As evident from Fig. 15, every framework except FAU has at least one Al T-site whose distribution of proton populations is more sensitive to temperature than the single unique T-site in CHA. In particular, more than half of the T-sites in MFI are expected to respond more sensitively to temperature than the single T-site in CHA. While observed IR spectra are convolutions of changes in these proton populations, and are further dependent on the changes in frequencies and intensities at each distinct proton location, these energetic differences among proton populations may underlie the origin the observed temperature dependences in OH stretching regions in IR spectra of many framework topologies [46–49].

In the case of the FAU topology, which contains a single unique T-site, Schoonheydt and Uytterhoeven measured IR spectra on Al-dense H-FAU zeolites (Si/Al = 1–5) and Na-H-FAU zeolites with approximately equimolar ratios of H^+ and Na^+ cations [47]. OH stretching features were observed at ~3550 cm^{-1} and ~3650 cm^{-1}, attributed to protons occupying sodalite cages and supercages, respectively. OH stretching intensities decreased reversibly with increasing temperature in these H-FAU samples, which are Al-dense and statistically likely to contain high fractions of Al-Al site pairs (and triples) in the same 6-MR [66]; these observations are reminiscent of those documented here on H-CHA zeo-

Table 5
First-order propane cracking rate constants (748 K, per H^+), activation energies, and activation entropies on Na-H-CHA zeolites.

Sample	H^+/H^+_{parent}	k_{app} [a]/10^{-3} mol (mol residual H^+) s^{-1} (bar C_3H_8) $^{-1}$	E_{app} [b]/kJ mol^{-1}	ΔS_{app} [c]/J mol^{-1} K^{-1}
Na_0H_{100}CHA (14.5, 0%)	1.00	0.4	164	−99
$Na_{47}H_{53}$CHA (14.5, 0%)	0.53	0.3	159	−108
$Na_{59}H_{41}$CHA (14.5, 0%)	0.41	0.3	162	−105
Na_0H_{100}CHA (15.0, 44%)	1.00	2.5	166	−80
$Na_{36}H_{64}$CHA (15.0, 44%)	0.64	0.5	166	−94
$Na_{55}H_{45}$CHA (15.0, 44%)	0.45	0.5	162	−99
$Na_{69}H_{31}$CHA (15.0, 44%)	0.31	0.3	166	−97

[a] Uncertainties are ±15%.
[b] Uncertainties are ±8 kJ mol^{-1}.
[c] Uncertainties are ±9 J mol^{-1} K^{-1}.

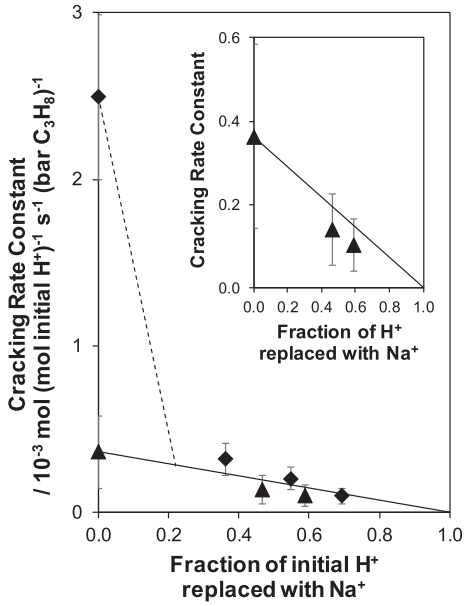

Fig. 14. Protolytic propane cracking rate constants (748 K, per initial H^+ site) on Na-H-CHA zeolites containing 0% Al (▲) and 44% Al in 6-MR pairs (◆), plotted as a function of the fraction of H^+ sites on the parent sample titrated by Na^+; inset shows magnification of data on the sample containing 0% Al in 6-MR pairs. Solid line represents apparent rate constant for isolated protons on H-CHA (14.5, 0%) and dashed line represents a prediction (to guide the eye) for the expected apparent rate constant on Na_xH_yCHA (15.0, 44%) samples if 6-MR paired protons were preferentially titrated by Na^+ prior to isolated protons.

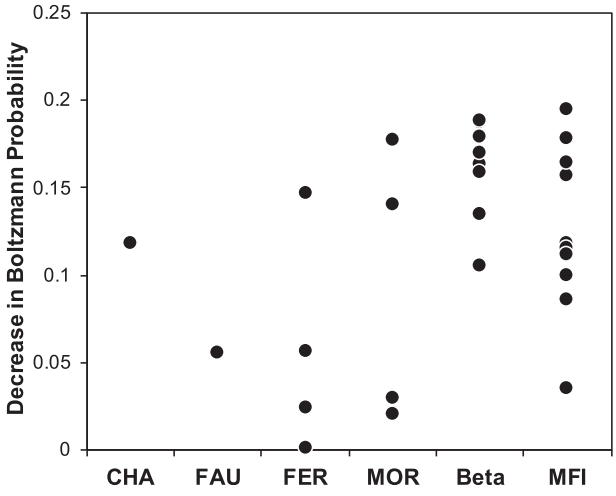

Fig. 15. Decrease in Boltzmann probability of the lowest energy isolated proton location from 448 K to 748 K for all possible T-sites in CHA, FAU, FER, MOR, Beta, and MFI zeolite frameworks. Data used to calculate the values in this figure were reported by Jones and Iglesia [52].

lites containing 6-MR Al pairs (Fig. 2a and b), as both CHA and FAU are constructed of the same double six-ring building units. OH IR spectra of Na-H-FAU, in which ~50% of the H^+ were replaced by Na^+, did not show the 3550 cm^{-1} feature, while the 3650 cm^{-1} feature became insensitive to temperature [47]. This observation suggests that Na^+ ions preferentially occupied the smaller available voids in FAU zeolites, consistent with similar conclusions in MOR that Na^+ cations preferentially exchange with protons in 8-MR voids than in larger 12-MR channels [4,67,68]. Here, we estimate a ~10 kJ mol^{-1} preference for Na^+ ions residing in 6-MR of CHA (Section S5, SI), consistent with these previous conclusions. We conclude that IR OH stretching vibrations of Na-H-CHA zeolites show a similar temperature sensitivity to H-CHA zeolites containing 6-MR Al-Al site pairs, because higher-energy Na^+-H^+ pair configurations have lower oscillator strengths, and the siting of such Na^+-H^+ pairs in CHA is influenced by the preference of larger Na^+ cations to reside within smaller rings.

Regarding protolytic alkane cracking catalysis, the systematic increase in propane cracking rate constants (per H^+) with 6-MR paired Al content (Fig. 13) reported here on H-CHA of fixed bulk Al content (Si/Al = 15) is reminiscent of the systematic increase in alkane cracking rate constants (per H^+) reported on H-MFI samples of increasing bulk Al content (Si/Al = 16–140) [14,18] and, on average, presumably increasing proximal Al content. The invariant apparent activation energies and systematically less negative activation entropies with increasing 6-MR paired Al content in H-CHA zeolites of fixed Si/Al ratio (Fig. S12, SI) reported here resemble the trends reported by Ding and co-workers on H-MFI samples with increasing paired Al content (measured by Co^{2+} titration) due to decreases in Si/Al ratio (140 to 16; E_{app} = 141–147 kJ mol^{-1}; ΔS_{app} = −101 to −87 J mol^{-1} K^{-1}) [14]. We note that similar trends in apparent activation energy and entropy values for protolytic alkane activation among H-MFI samples of decreasing Si/Al ratio have also been measured independently by Bell and co-workers, but instead attributed to increasing fractions of Al and charge-compensating protons confined with larger MFI channel intersection voids (inferred from UV–Visible spectra on Co^{2+}-form MFI samples) [18], wherein less restrictive confinement confers entropic stabilization to the carbonium ion-like transition states involved. We further note that interpretations regarding the intrazeolitic void locations surveyed by Co^{2+} titrants are inextricably linked to the location of proximal Al-Al lattice ensembles that bind them, and therefore report incompletely on the distribution of all Al sites (including isolated Al) among distinct void environments. Thus, precise mechanistic interpretations of kinetic data in MFI zeolites have remained elusive, challenged both by the lack of a precise definition of the Al-Al site pair configurations titrated by Co^{2+} [17] and the convolved influences of acid site proximity and location among different void environments [13]. We surmise

that proton proximity may also influence high temperature protolytic alkane cracking and dehydrogenation rates on other zeolite topologies that have not been studied in as much detail as MFI, but for which effects of acid site proximity remain convolved with those of varying acid site location within distinct void environments.

Finally, Na^+ cations are shown here by experiment and theory to preferentially titrate H^+ sites in 6-MR Al-Al site pair configurations over isolated Al sites in CHA frameworks, leading to a sharp decrease in propane cracking rate constants (748 K, per residual H^+) upon Na^+ poisoning of H-CHA samples that contain 6-MR paired Al sites (Fig. 14). At first glance, these findings appear reminiscent of the strong Na^+ poisoning effects in FAU-type zeolites for hydrocarbon cracking reactions [69–71]; however, later studies of steam- and chemically-dealuminated FAU samples showed equimolar titration of all H^+ sites by Na^+, suggesting that all proton sites in a given FAU sample were equivalent in reactivity [50]. We surmise that observations of strong Na^+ titration effects in aluminosilicate zeolites, in certain cases wherein replacement of a minority of the H^+ sites present initially is observed to suppress the majority of observed reactivity [72], may reflect an underlying influence of acid site pairs on catalysis.

4. Conclusions

The equilibrium distribution of protons among crystallographically-distinct O atoms in CHA zeolites depends on the local arrangement of Al heteroatoms, which influences their OH IR spectra and catalytic behavior for protolytic alkane activation. Each of the four distinct lattice O atoms in CHA zeolites can be characterized by the size of the three siloxane rings it occupies, which contain four, six, or eight constituent T-atoms. DFT calculations indicate that OH stretching vibrations observed experimentally at ~3600 cm^{-1} reflect protons at the 844 O site, while those at ~3580 cm^{-1} reflect contributions from protons at the 644, 864, 884 O sites. The latter vibration arises from protons in both 6-MR and 8-MR environments, in contradiction to prior interpretations that OH vibrations at 3600 cm^{-1} and 3575 cm^{-1} respectively reflect protons pointing into the 8-MR and 6-MR of CHA, as inferred from neutron diffraction data collected at 5 K. Protons that compensate 6-MR isolated Al sites are isoenergetic (within 10 kJ/mol) and thus show similar probabilities (<10% variation) to occupy any of the four O atoms in CHA over a wide temperature range (448–748 K). In contrast, protons that compensate 6-MR paired Al sites vary in energy (by up to 40 kJ/mol), with higher energy configurations characterized by lower oscillator strengths that result in lower molar absorptivities. Such higher energy proton configurations become progressively populated with increasing temperature and cause a reversible decrease in integrated areas for OH IR features, interpreted previously to proton delocalization from lattice O atoms at higher temperatures. This interpretation, however, is inconsistent with the temperature-insensitive OH peak areas measured experimentally on H-CHA zeolites containing only isolated Al sites that give rise to essentially invariant proton populations in the temperature range studied. These findings indicate that OH IR stretching vibrations should change with temperature in lower-symmetry zeolite frameworks and those with different Al-Al site pair arrangements, as long as distinct OH groups possess different oscillator strengths and differ in relative energy.

First-order rate constants for protolytic propane cracking (748 K, per H^+) increase systematically with the fraction of 6-MR paired sites among H-CHA zeolites, behavior that is brought into sharp relief from interrogating samples of essentially fixed composition (Si/Al = 15). Rate constants are ~12× higher on paired than isolated protons, despite similar apparent activation energies on these site ensembles, because of less negative apparent activation entropies on paired proton sites that entropically stabilize the late carbonium ion-like transition states involved in protolytic cracking. These findings are consistent with prior interpretations of higher *n*-alkane cracking and dehydrogenation rates on lower-symmetry H-MFI zeolites of varying bulk composition proposed also to reflect differences in proton proximity [14], although similar observations have been independently attributed to reflect the location of protons among different voids [18], motivating further investigations of proton proximity effects on catalysis by MFI and other zeolite topologies. Additionally, Na^+ cations are shown by experiment and theory to preferentially titrate H^+ sites in 6-MR Al-Al site pair configurations than isolated Al sites in CHA frameworks, leading to a sharp decrease in propane cracking rate constants (748 K, per residual H^+) upon Na^+-poisoning of H-CHA samples that contain 6-MR paired Al sites, motivating further research into the potential use of cation poisoning as a method to detect differences in reactivity among the various Al-Al site pair arrangements present in a given zeolite sample.

The demonstration that rate constants (per H^+) of alkane activation catalysis are higher on 6-MR paired acid sites than isolated acid sites in CHA zeolites, via entropic stabilization of the late carbonium-ion-like transition states formed in protolytic mechanisms, extend our prior reports of such higher turnover rates (per H^+) for methanol [21] and ethanol [8] dehydration to form their corresponding ether products. In the case of alkanol dehydration catalysis, kinetically relevant transition states are preferentially stabilized by specific hydrogen bonding interactions with co-adsorbed alkanols at the second Al site in a 6-MR paired configuration. Thus, the data presented herein constitute evidence that Al-Al pair site ensembles can accelerate two distinct types of Brønsted acid-mediated catalytic cycles, both alkanol dehydration that prevails at low temperatures (<500 K) via polar oxygenated transition states that benefit strongly from hydrogen bonding interactions with their surrounding environment, and alkane activation that prevails at much higher temperatures (>700 K) via non-polar hydrocarbon transition states that are influenced by van der Waals interactions with their confining environment. This behavior is all the more prominent in the case of single T-site zeolite (CHA) materials of fixed elemental composition, heralding the even richer catalytic diversity among zeolites with varying atomic Al arrangement that also differ in topology and composition.

5. Data statement

Structure files and key values from all the DFT calculations are available for download via the Supplementary Information. This folder includes the CONTCARs provided by VASP after geometry optimization for isolated and paired (3NN 6-MR, 3NN 8-MR, and 4NN 8-MR) Al-H form structures, and isolated and paired (3NN 6-MR) Al-Na form structures. These CONTCARs were used to perform the vibrational analyses.

Declaration of Competing Interest

The authors declare that they have no known competing financial interests or personal relationships that could have appeared to influence the work reported in this paper.

Acknowledgements

We acknowledge financial support provided by the National Science Foundation under Cooperative Agreement No. EEC-1647722, which is an Engineering Research Center for the Innova-

tive and Strategic Transformation of Alkane Resources. JTC thanks the Arthur J. Schmitt Foundation for financial aid in the form of a PhD fellowship. We thank Dr. John R. Di Iorio and Claire T. Nimlos for helpful technical discussions. We also thank Sachem, Inc. for providing the organic structure-directing agent used to synthesize SSZ-13. This research was supported in part by the Notre Dame Center for Research Computing through access to high performance computing clusters.

Appendix A. Supplementary material

Supplementary data to this article can be found online at https://doi.org/10.1016/j.jcat.2020.12.038.

References

[1] M.M. Mestdagh, W.E. Stone, J.J. Fripiat, Proton mobility in solids. IV. Study of proton motion in the decationated Y zeolite by nuclear magnetic resonance, J. Phys. Chem. 76 (1972) 1220–1226, https://doi.org/10.1021/j100652a023.
[2] P. Sarv, T. Tuherm, E. Lippmaa, K. Keskinen, A. Root, Mobility of the acidic proton in Brønsted sites of H-Y, H-Mordenite, and H-ZSM-5 zeolites, studied by high-temperature ^{1}H MAS NMR, J. Phys. Chem. 99 (1995) 13763–13768, https://doi.org/10.1021/j100038a003.
[3] J. Dědeček, Z. Sobalík, B. Wichterlová, Siting and distribution of framework aluminium atoms in silicon-rich zeolites and impact on catalysis, Catal. Rev. 54 (2012) 135–223, https://doi.org/10.1080/01614940.2012.632662.
[4] A. Bhan, A.D. Allian, G.J. Sunley, D.J. Law, E. Iglesia, Specificity of sites within eight-membered ring zeolite channels for carbonylation of methyls to acetyls, J. Am. Chem. Soc. 129 (2007) 4919–4924, https://doi.org/10.1021/ja070094d.
[5] R. Gounder, E. Iglesia, Catalytic consequences of spatial constraints and acid site location for monomolecular alkane activation on zeolites, J. Am. Chem. Soc. 131 (2009) 1958–1971, https://doi.org/10.1021/ja808292c.
[6] R. Gounder, E. Iglesia, The catalytic diversity of zeolites: confinement and solvation effects within voids of molecular dimensions, Chem. Commun. 49 (2013) 3491, https://doi.org/10.1039/c3cc40731d.
[7] E.G. Derouane, M.E. Davis, On the polarizability of molecular sieves: ^{129}Xe NMR chemical shifts and sorption energetics, J. Mol. Catal. 48 (1988) 37–41, https://doi.org/10.1016/0304-5102(88)85126-5.
[8] A.J. Hoffman, J.S. Bates, J.R. Di Iorio, S.V. Nystrom, C.T. Nimlos, R. Gounder, D. Hibbitts, Rigid arrangements of ionic charge in zeolite frameworks conferred by specific aluminum distributions preferentially stabilize alkanol dehydration transition states, Angew. Chem. Int. Ed. 59 (2020) 2–11, https://doi.org/10.1002/anie.202007790.
[9] J.S. Bates, B.C. Bukowski, J. Greeley, R. Gounder, Structure and solvation of confined water and water–ethanol clusters within microporous Brønsted acids and their effects on ethanol dehydration catalysis, Chem. Sci. 11 (2020) 7102–7122, https://doi.org/10.1039/D0SC02589E.
[10] Y. Román-Leshkov, M. Moliner, M.E. Davis, Impact of controlling the site distribution of Al atoms on catalytic properties in ferrierite-type zeolites, J. Phys. Chem. C. 115 (2011) 1096–1102, https://doi.org/10.1021/jp106247g.
[11] M. Neurock, Engineering molecular transformations for sustainable energy conversion, Ind. Eng. Chem. Res. 49 (2010) 10183–10199, https://doi.org/10.1021/ie101300c.
[12] M. Boronat, C. Martínez, A. Corma, Mechanistic differences between methanol and dimethyl ether carbonylation in side pockets and large channels of mordenite, Phys. Chem. Chem. Phys. 13 (2011) 2603, https://doi.org/10.1039/c0cp01996h.
[13] B.C. Knott, C.T. Nimlos, D.J. Robichaud, M.R. Nimlos, S. Kim, R. Gounder, Consideration of the aluminum distribution in zeolites in theoretical and experimental catalysis research, ACS Catal. 8 (2018) 770–784, https://doi.org/10.1021/acscatal.7b03676.
[14] C. Song, Y. Chu, M. Wang, H. Shi, L. Zhao, X. Guo, W. Yang, J. Shen, N. Xue, L. Peng, W. Ding, Cooperativity of adjacent Brønsted acid sites in MFI zeolite channel leads to enhanced polarization and cracking of alkanes, J. Catal. 349 (2017) 163–174, https://doi.org/10.1016/j.jcat.2016.12.024.
[15] A.N. Mlinar, P.M. Zimmerman, F.E. Celik, M. Head-Gordon, A.T. Bell, Effects of Brønsted-acid site proximity on the oligomerization of propene in H-MFI, J. Catal. 288 (2012) 65–73, https://doi.org/10.1016/j.jcat.2012.01.002.
[16] M. Bernauer, E. Tabor, V. Pashkova, D. Kaucký, Z. Sobalík, B. Wichterlová, J. Dedecek, Proton proximity – New key parameter controlling adsorption, desorption and activity in propene oligomerization over H-ZSM-5 zeolites, J. Catal. 344 (2016) 157–172, https://doi.org/10.1016/j.jcat.2016.09.025.
[17] C.T. Nimlos, A.J. Hoffman, Y. Gul Hur, B. Jin Lee, J.R. Di Iorio, D. Hibbitts, R. Gounder, Experimental and theoretical assessments of aluminum proximity in MFI zeolites and its alteration by organic and inorganic structure-directing agents, Chem. Mater. (2020), https://doi.org/10.1021/acs.chemmater.0c03154.
[18] A. Janda, A.T. Bell, Effects of Si/Al ratio on the distribution of framework Al and on the rates of alkane monomolecular cracking and dehydrogenation in H-MFI, J. Am. Chem. Soc. 135 (2013) 19193–19207, https://doi.org/10.1021/ja4081937.
[19] J.R. Di Iorio, S. Li, C.B. Jones, C.T. Nimlos, Y. Wang, E. Kunkes, V. Vattipalli, S. Prasad, A. Moini, W.F. Schneider, R. Gounder, Cooperative and competitive occlusion of organic and inorganic structure-directing agents within chabazite zeolites influences their aluminum arrangement, J. Am. Chem. Soc. 142 (2020) 4807–4819, https://doi.org/10.1021/jacs.9b13817.
[20] J.R. Di Iorio, R. Gounder, Controlling the isolation and pairing of aluminum in chabazite zeolites using mixtures of organic and inorganic structure-directing agents, Chem. Mater. 28 (2016) 2236–2247, https://doi.org/10.1021/acs.chemmater.6b00181.
[21] J.R. Di Iorio, C.T. Nimlos, R. Gounder, Introducing catalytic diversity into single-site chabazite zeolites of fixed composition via synthetic control of active site proximity, ACS Catal. 7 (2017) 6663–6674, https://doi.org/10.1021/acscatal.7b01273.
[22] F. Göltl, A.M. Love, S.C. Schuenzel, P. Wolf, M. Mavrikakis, I. Hermans, Computational description of key spectroscopic features of zeolite SSZ-13, Phys. Chem. Chem. Phys. 21 (2019) 19065–19075, https://doi.org/10.1039/C9CP03146D.
[23] T.R. Hughes, H.M. White, A study of the surface structure of decationized Y zeolite by quantitative infrared spectroscopy, J. Phys. Chem. 71 (1967) 2192–2201, https://doi.org/10.1021/j100866a035.
[24] P.A. Jacobs, W.J. Mortier, An attempt to rationalize stretching frequencies of lattice hydroxyl groups in hydrogen-zeolites, Zeolites. 2 (1982) 226–230, https://doi.org/10.1016/S0144-2449(82)80056-0.
[25] C.A. Emeis, Determination of integrated molar extinction coefficients for infrared absorption bands of pyridine adsorbed on solid acid catalysts, J. Catal. 141 (1993) 347–354, https://doi.org/10.1006/jcat.1993.1145.
[26] M.A. Makarova, V.L. Zholobenko, K.M. Al-Ghefaili, N.E. Thompson, J. Dewing, J. Dwyer, Brønsted acid sites in zeolites. FTIR study of molecular hydrogen as a probe for acidity testing, J. Chem. Soc., Faraday Trans. 90 (1994) 1047–1054, https://doi.org/10.1039/FT9949001047.
[27] M.A. Makarova, A.E. Wilson, B.J. van Liemt, C.M.A.M. Mesters, A.W. de Winter, C. Williams, Quantification of Brønsted acidity in mordenites, J. Catal. 172 (1997) 170–177, https://doi.org/10.1006/jcat.1997.1849.
[28] S. Bordiga, C. Lamberti, F. Bonino, A. Travert, F. Thibault-Starzyk, Probing zeolites by vibrational spectroscopies, Chem. Soc. Rev. 44 (2015) 7262–7341, https://doi.org/10.1039/C5CS00396B.
[29] H. Tsubomura, Nature of the hydrogen bond. III. The measurement of the infrared absorption intensities of free and hydrogen-bonded OH bands. Theory of the increase of the intensity due to the hydrogen bond, J. Chem. Phys. 24 (1956) 927–931, https://doi.org/10.1063/1.1742717.
[30] B. Athokpam, S.G. Ramesh, R.H. McKenzie, Effect of hydrogen bonding on the infrared absorption intensity of OH stretch vibrations, Chem. Phys. 488–489 (2017) 43–54, https://doi.org/10.1016/j.chemphys.2017.03.006.
[31] L.J. Smith, A. Davidson, A.K. Cheetham, A neutron diffraction and infrared spectroscopy study of the acid form of the aluminosilicate zeolite, chabazite (H-SSZ-13), Catal. Lett. 49 (1997) 143–146, https://doi.org/10.1023/A:1019097019846.
[32] S.A. Bates, W.N. Delgass, F.H. Ribeiro, J.T. Miller, R. Gounder, Methods for NH3 titration of Brønsted acid sites in Cu-zeolites that catalyze the selective catalytic reduction of NOx with NH3, J. Catal. 312 (2014) 26–36, https://doi.org/10.1016/j.jcat.2013.12.020.
[33] J.R. Di Iorio, S.A. Bates, A.A. Verma, W.N. Delgass, F.H. Ribeiro, J.T. Miller, R. Gounder, The dynamic nature of Brønsted acid sites in Cu–Zeolites during NOx selective catalytic reduction: quantification by gas-phase ammonia titration, Top. Catal. 58 (2015) 424–434, https://doi.org/10.1007/s11244-015-0387-8.
[34] P.M. Kester, J.T. Miller, R. Gounder, Ammonia titration methods to quantify Brønsted acid sites in zeolites substituted with aluminum and boron heteroatoms, Ind. Eng. Chem. Res. 57 (2018) 6673–6683, https://doi.org/10.1021/acs.iecr.8b00933.
[35] V.J. Cybulskis, J.W. Harris, Y. Zvinevich, F.H. Ribeiro, R. Gounder, A transmission infrared cell design for temperature-controlled adsorption and reactivity studies on heterogeneous catalysts, Rev. Sci. Instrum. 87 (2016), https://doi.org/10.1063/1.4963665 103101.
[36] S. Prodinger, H. Shi, S. Eckstein, J.Z. Hu, M.V. Olarte, D.M. Camaioni, M.A. Derewinski, J.A. Lercher, Stability of zeolites in aqueous phase reactions, Chem. Mater. 29 (2017) 7255–7262, https://doi.org/10.1021/acs.chemmater.7b01847.
[37] J.W. Harris, M.J. Cordon, J.R. Di Iorio, J.C. Vega-Vila, F.H. Ribeiro, R. Gounder, Titration and quantification of open and closed Lewis acid sites in Sn-Beta zeolites that catalyze glucose isomerization, J. Catal. 335 (2016) 141–154, https://doi.org/10.1016/j.jcat.2015.12.024.
[38] G. Kresse, J. Furthmüller, Efficient iterative schemes for *ab initio* total-energy calculations using a plane-wave basis set, Phys. Rev. B. 54 (1996) 11169–11186, https://doi.org/10.1103/PhysRevB.54.11169.
[39] J.P. Perdew, K. Burke, M. Ernzerhof, Generalized gradient approximation made simple, Phys. Rev. Lett. 77 (1996) 3865–3868, https://doi.org/10.1103/PhysRevLett.77.3865.
[40] G. Kresse, D. Joubert, From ultrasoft pseudopotentials to the projector augmented-wave method, Phys. Rev. B. 59 (1999) 1758–1775, https://doi.org/10.1103/PhysRevB.59.1758.
[41] P.E. Blöchl, Projector augmented-wave method, Phys. Rev. B. 50 (1994) 17953–17979, https://doi.org/10.1103/PhysRevB.50.17953.
[42] Ch. Baerlocher, L.B. McCusker, Database of Zeolite Structures, (n.d.). http://www.iza-structure.org/databases/ (accessed October 4, 2020).
[43] X. Gonze, C. Lee, Dynamical matrices, Born effective charges, dielectric permittivity tensors, and interatomic force constants from density-functional

perturbation theory, Phys. Rev. B. 55 (1997) 10355–10368, https://doi.org/10.1103/PhysRevB.55.10355.
[44] A. Hjorth Larsen, J. Jørgen Mortensen, J. Blomqvist, I.E. Castelli, R. Christensen, M. Dułak, J. Friis, M.N. Groves, B. Hammer, C. Hargus, E.D. Hermes, P.C. Jennings, P. Bjerre Jensen, J. Kermode, J.R. Kitchin, E. Leonhard Kolsbjerg, J. Kubal, K. Kaasbjerg, S. Lysgaard, J. Bergmann Maronsson, T. Maxson, T. Olsen, L. Pastewka, A. Peterson, C. Rostgaard, J. Schiøtz, O. Schütt, M. Strange, K.S. Thygesen, T. Vegge, L. Vilhelmsen, M. Walter, Z. Zeng, K.W. Jacobsen, The atomic simulation environment—a Python library for working with atoms, J. Phys. Condens. Matter. 29 (2017), https://doi.org/10.1088/1361-648X/aa680e 273002.
[45] A. Janin, M. Maache, J.C. Lavalley, J.F. Joly, F. Raatz, N. Szydlowski, FT i.r. study of the silanol groups in dealuminated HY zeolites: nature of the extraframework debris, Zeolites. 11 (1991) 391–396, https://doi.org/10.1016/0144-2449(91)80308-M.
[46] J. Ward, The nature of active sites on zeolites II. Temperature dependence of the infrared spectra of hydrogen Y zeolite, J. Catal. 9 (1967) 396–402, https://doi.org/10.1016/0021-9517(67)90266-7.
[47] R. Schoonheydt, Influence of temperature on the OH-band intensity in the infrared spectra of decationated zeolites X and Y, J. Catal. 19 (1970) 55–63, https://doi.org/10.1016/0021-9517(70)90296-4.
[48] P.A. Jacobs, J.B. Uytterhoeven, Assignment of the hydroxyl bands in the infrared spectra of zeolites X and Y. Part 1. —Na—H zeolites, J. Chem. Soc., Faraday Trans. 1 (69) (1973) 359, https://doi.org/10.1039/f19736900373.
[49] R. Osuga, T. Yokoi, K. Doitomi, H. Hirao, J.N. Kondo, Infrared investigation of dynamic behavior of brønsted acid sites on zeolites at high temperatures, J. Phys. Chem. C. 121 (2017) 25411–25420, https://doi.org/10.1021/acs.jpcc.7b09846.
[50] R. Gounder, A.J. Jones, R.T. Carr, E. Iglesia, Solvation and acid strength effects on catalysis by faujasite zeolites, J. Catal. 286 (2012) 214–223, https://doi.org/10.1016/j.jcat.2011.11.002.
[51] S. Li, H. Li, R. Gounder, A. Debellis, I.B. Müller, S. Prasad, A. Moini, W.F. Schneider, First-principles comparison of proton and divalent copper cation exchange energy landscapes in SSZ-13 zeolite, J. Phys. Chem. C. 122 (2018) 23564–23573, https://doi.org/10.1021/acs.jpcc.8b07213.
[52] A.J. Jones, E. Iglesia, The strength of Brønsted acid sites in microporous aluminosilicates, ACS Catal. 5 (2015) 5741–5755, https://doi.org/10.1021/acscatal.5b01133.
[53] S. Nystrom, A. Hoffman, D. Hibbitts, Tuning Brønsted acid strength by altering site proximity in CHA framework zeolites, ACS Catal. 8 (2018) 7842–7860, https://doi.org/10.1021/acscatal.8b02049.
[54] T.F. Narbeshuber, H. Vinek, J.A. Lercher, Monomolecular conversion of light alkanes over H-ZSM-5, J. Catal. 157 (1995) 388–395, https://doi.org/10.1006/jcat.1995.1304.
[55] W.O. Haag, R.M. Dessau, in: Proc 8th Int Congr Catal, Berlin, 1984, p. 305.
[56] S.M. Babitz, B.A. Williams, J.T. Miller, R.Q. Snurr, W.O. Haag, H.H. Kung, Monomolecular cracking of n-hexane on Y, MOR, and ZSM-5 zeolites, Appl. Catal. Gen. 179 (1999) 71–86, https://doi.org/10.1016/S0926-860X(98)00301-9.
[57] S. Kotrel, H. Knözinger, B.C. Gates, The Haag-Dessau mechanism of protolytic cracking of alkanes, Microporous Mesoporous Mater. 35–36 (2000) 11–20, https://doi.org/10.1016/S1387-1811(99)00204-8.
[58] P.M. Kester, E. Iglesia, R. Gounder, Parallel alkane dehydrogenation routes on Brønsted acid and reaction-derived carbonaceous active sites in zeolites, J. Phys. Chem. C. 124 (2020) 15839–15855, https://doi.org/10.1021/acs.jpcc.0c01808.
[59] J.H. Yun, R.F. Lobo, Effects of temperature pretreatment on propane cracking over H-SSZ-13 zeolites, Catal. Sci. Technol. 5 (2015) 264–273, https://doi.org/10.1039/C4CY00731J.
[60] R.A. van Santen, G.J. Kramer, Reactivity theory of zeolitic Brønsted acidic sites, Chem. Rev. 95 (1995) 637–660, https://doi.org/10.1021/cr00035a008.
[61] A.M. Rigby, G.J. Kramer, R.A. van Santen, Mechanisms of hydrocarbon conversion in zeolites: a quantum mechanical study, J. Catal. 170 (1997) 1–10, https://doi.org/10.1006/jcat.1997.1574.
[62] S.A. Zygmunt, L.A. Curtiss, P. Zapol, L.E. Iton, Ab initio and density functional study of the activation barrier for ethane cracking in cluster models of zeolite H-ZSM-5, J. Phys. Chem. B. 104 (2000) 1944–1949, https://doi.org/10.1021/jp993194h.
[63] M.V. Frash, R.A. van Santen, Quantum-chemical modeling of the hydrocarbon transformations in acid zeolite catalysts, Top. Catal. 9 (1999) 191–205, https://doi.org/10.1023/A:1019183110705.
[64] R. Gounder, E. Iglesia, The roles of entropy and enthalpy in stabilizing ion-pairs at transition states in zeolite acid catalysis, Acc. Chem. Res. 45 (2012) 229–238, https://doi.org/10.1021/ar200138n.
[65] M. Boudart, Turnover rates in heterogeneous catalysis, Chem. Rev. 95 (1995) 661–666, https://doi.org/10.1021/cr00035a009.
[66] S.A. Bates, A.A. Verma, C. Paolucci, A.A. Parekh, T. Anggara, A. Yezerets, W.F. Schneider, J.T. Miller, W.N. Delgass, F.H. Ribeiro, Identification of the active Cu site in standard selective catalytic reduction with ammonia on Cu-SSZ-13, J. Catal. 312 (2014) 87–97, https://doi.org/10.1016/j.jcat.2014.01.004.
[67] V.A. Veefkind, M.L. Smidt, J.A. Lercher, On the role of strength and location of Brønsted acid sites for ethylamine synthesis on mordenite catalysts, Appl. Catal. Gen. 194–195 (2000) 319–332, https://doi.org/10.1016/S0926-860X(99)00378-6.
[68] M. Maache, A. Janin, J.C. Lavalley, E. Benazzi, FT infrared study of Brønsted acidity of H-mordenites: heterogeneity and effect of dealumination, Zeolites. 15 (1995) 507–516, https://doi.org/10.1016/0144-2449(95)00019-3.
[69] R.A. Beyelein, G.B. McVicker, L.N. Yacullo, J.J. Ziemiak, Abstr. Pap.-Am. Chem. Soc. (1986) 190.
[70] P. Fritz, The effect of sodium poisoning on dealuminated Y-type zeolites, J. Catal. 118 (1989) 85–98, https://doi.org/10.1016/0021-9517(89)90303-5.
[71] D. Barthomeuf, X, Y, aluminum-deficient, and ultrastable faujasite-type zeolites III. Catalytic activity, J. Catal. 30 (1973) 288–297, https://doi.org/10.1016/0021-9517(73)90076-6.
[72] J.A. van Bokhoven, B.A. Williams, W. Ji, D.C. Koningsberger, H.H. Kung, J.T. Miller, Observation of a compensation relation for monomolecular alkane cracking by zeolites: the dominant role of reactant sorption, J. Catal. 224 (2004) 50–59, https://doi.org/10.1016/j.jcat.2004.02.003.